UNIVERSIDADE
BEIRA INTERIOR

Refractory ceramics in the context of the fabrication of rocket nozzles:

Conventional alumina and industrial waste alumina-silicate refractory compositions.

(Versão final após defesa)

João Gomes Portugal da Fonseca

Dissertação para obtenção do Grau de Mestre em

Engenharia Aeronáutica

(Mestrado integrado)

Orientador: Prof. Doutor Abílio Manuel Pereira da Silva

Co-orientador: Prof. Doutor Francisco Miguel Ribeiro Proença Brojo

Março 2023

Declaração de Integridade

Eu, João Gomes Portugal da Fonseca, que abaixo assino, estudante com o número de inscrição a38982 de/o Mestrado Integrado em Engenharia Aeronáutica da Faculdade de Engenharia, declaro ter desenvolvido o presente trabalho e elaborado o presente texto em total consonância com o **Código de Integridades da Universidade da Beira Interior**.

Mais concretamente afirmo não ter incorrido em qualquer das variedades de Fraude Académica, e que aqui declaro conhecer, que em particular atendi à exigida referenciação de frases, extratos, imagens e outras formas de trabalho intelectual, e assumindo assim na íntegra as responsabilidades da autoria.

Universidade da Beira Interior, Covilhã 27/03 /2023

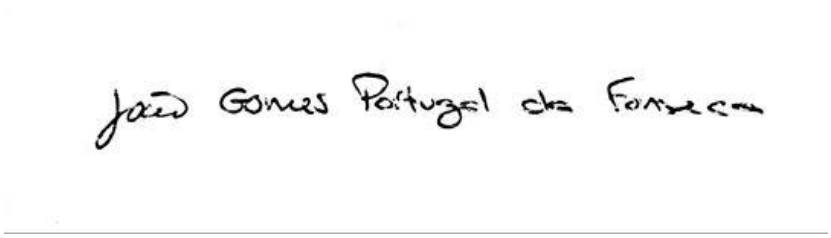

Dedicatória

Esta dissertação é dedicada à minha mãe, Ana, ao meu Pai, João e à minha irmã, Sofia, a quem agradeço a pessoa que sou hoje, e de quem o apoio incondicional, confiança e orgulho me propulsionaram pelos caminhos que ultimamente me levaram a este ponto da minha vida.

Ao meu primo Christian deixo uma palavra de reconhecimento pelo esforço que fez para garantir que eu me encontrava a trabalhar nesta dissertação independentemente da hora do dia e de agradecimento pela honra que é ter a sua amizade e camaradagem inquebráveis.

Ao meu afilhado Santiago que me abençoou com o orgulho de o apadrinhar durante o desenvolvimento deste trabalho e à sua irmã Matilde.

Dedico esta dissertação também aos meus avós maternos e paternos, aos meus tios, tias e primos, e à minha madrinha, pelos valores que me incutiram.

Esta dissertação é também, em parte, um trabalho vosso.

Agradecimentos

Gostaria de agradecer em primeiro lugar ao Professor Doutor Abílio Manuel Pereira Silva por me apresentar a possibilidade de desenvolver este cativante tema, pelo apoio incansável durante o desenvolvimento do mesmo, pela confiança em mim depositada e pela sua disponibilidade infindável.

Ao Professor Doutor Francisco Miguel Ribeiro Proença Brojo, sem quem a oportunidade de desenvolver o tema deste trabalho não existiria.

À Universidade da Beira Interior, em particular, a todos os membros do Departamento de Ciências Aeroespaciais e do Departamento de Engenharia Eletromecânica, pelos conhecimentos, informação e meios disponibilizados ao longo do meu percurso de formação.

Ao C-MAST|UBI (Centre for Mechanical and Aerospace Science and Technologies) pela disponibilização de equipamentos, recursos, matérias-primas e todo o tipo de meios laboratoriais. Assim como ao FabLab|UBI, em particular ao Sr. Nuno dos Santos, pelo apoio no processo de impressão 3D.

Pelo fornecimento das matérias-primas provenientes das minas reutilizadas neste trabalho queria agradecer ao projeto RecMine – Environmental footprint reduction trough eco-friendly technologies of mine tailings recycling; Funding: ERA-MIN Joint Call 2021 on Raw Materials for the Sustainable Development and Circular Economy.

Finalmente, um especial agradecimento à minha família e amigos, pelo apoio e motivação dados não só ao longo deste trabalho, mas de todo o percurso que o precede.

Resumo

Devido à possibilidade de voltar a levar o ser humano à lua, ao aparecimento de voos comerciais em alta atmosfera e outos recentes desenvolvimentos, tem havido um renovado interesse na exploração espacial. No centro do que são as capacidades espaciais do ser humano estão os veículos utilizados para atingir a órbita terrestre e destinos mais além, estes veículos são compostos por uma multitude de partes, as quais devem ser cuidadosamente estudadas e desenvolvidas tendo em conta vários fatores. Neste trabalho, o bocal propulsivo do motor foguete é o ponto focal, com especial atenção aos materiais utilizados. Tradicionalmente composto por ligas metálicas, o bocal está sujeito a ambientes térmicos extremos, os quais impõem dificuldades aos materiais utilizados, tais como a oxidação dos mesmos. Adicionalmente as indústrias aeronáutica e aeroespacial são inerentemente dispendiosas, monetária e ambientalmente. Do modo que, neste trabalho, é estudado o uso não só de cerâmicas refratárias como uma alternativa às ligas metálicas tradicionalmente utilizadas na fabricação de tubeiras propulsivas, como também a utilização de cerâmicas refratárias compostas por materiais reutilizados, excedentes das minas da Panasqueira e cinzas provenientes da central termoelétrica do Pego, que seriam de outra maneira desaproveitados. Ao estudar estes materiais brutos, apercebemo-nos das possibilidades que estes apresentam, uma vez que são maioritariamente compostos por materiais como SiO_2 e Al_2O_3 usualmente utilizados em cerâmicas refratárias, inclusive cerâmicas refratárias presentes em casos de estudo semelhantes ao pretendido neste trabalho. O processo de manufatura, e os desafios em si inerentes, são discutidos e o produto final composto pelas cinzas e areias das minas é comparado com a cerâmica composta quase na sua totalidade por alumina. Os resultados demonstram que ao utilizar os materiais reutilizados existem algumas perdas em propriedades, como esperado. No entanto, cerâmicas refratárias capazes podem ser consistentemente fabricadas utilizando estes materiais.

Palavras-chave

Propulsão foguete; Al_2O_3; cerâmicas refratárias; bocal propulsivo; modelos de empacotamento de partículas; impressão 3D; fabrico de molde; resíduos minerais; porosidade; propriedades mecânicas; sinterização.

Abstract

Space exploration has had a regrowth in interest as the possibility for landing man on the moon returns following the appearance of commercial flights to high orbit among other recent developments. At the centre of the space capabilities of the human race are the vehicles it uses to achieve orbit and destinations beyond, these powerful vehicles are composed of many parts, and each must be studied and developed with various factors in mind. In this study the nozzle of the rocket engines, that quite literally power the human capability to explore space, are the focal point, specifically the materials used in these components. Traditionally composed of metallic alloys, the rocket nozzles are subject to extreme thermal environments, that lead to challenges such as the oxidation of the materials. Furthermore, the space exploration industry in inherently wasteful and costly, as well as rather environmentally unfavourable. In this study, therefore, a different approach is presented, in which refractory ceramics are studied as an alternative material for rocket nozzles, but also refractory ceramics composed of reutilized by-products of mines and thermoelectric centrals, materials that would by otherwise considered waste and disregarded. A closer look to these unrefined materials shows promise in its capabilities, as these are mainly composed by materials usually utilized in traditional refractory ceramics, and moreover in ceramics presented in study cases for rocket nozzle applications, like SiO_2 and Al_2O_3. The manufacturing process and challenges of such an approach are studied and discussed and the final refractory ceramic of fly-ash and mines sands are compared with and almost pure Al_2O_3 ceramic benchmark. The results indicate that by utilizing unrefined products losses in properties will be expected. However, capable ceramics are still consistently achievable using these alternative materials.

Keywords

Rocket propulsion, Al_2O_3; refractory ceramics; rocket nozzle; particle packing models; 3D printing; mould fabrication; mineral residues; porosity; mechanical properties; sintering.

Indice

Figure List

Tables List

Acronyms List

ACRONYMS

AFNOR	Association Française of Standardalization
ALU	Alumina samples identifier
ASH	Pego thermoelectric fly-ash identifier
ASTM	American Society for Testing and Materials
AT	Tabular alumina
AZS	Alumina-Zirconia-Silica
CA 25	Calcium aluminate cement with 80% alumina
CAD	Computer Aided Design
CFRP	Carbon Fibre Reinforced Polymers
CMC	Ceramic Matrix Composite
CPFT	Cumulative percentage finer than
CT 3000	Reactive alumina CT 3000 LS SG
EMMA	Elkem materials mix analyser
FI	Flow Index
MMC	Metal Matrix Composite
PA	Panasqueria waste and Pego fly-ash sample identifier
PAN	Panasqueira mines waste material identifier
PCE	Pyrometric Cone Equivalent
PEEK	Polyether Ether Ketone
PLC	Permanent Linear Change
PMC	Polymer Matrix Composite
RUL	Refractoriness Under Load
SSTO	Single Stage to Orbit
TBC	Thermal Barrier Coating
TPS	Thermal Protection System
UHTC	Ultra-High Temperature Ceramic
UHTCMC	Ultra-High Temperature Ceramic Matrix Composite

CHEMICAL FORMULAS

Al_2O_3	Alumina
AlN	Aluminium nitride
C	Carbon
CaO	Calcium oxide
CO	Carbon monoxide
Cr_2O_3	Chromium oxide
Fe_2O_3	Iron oxide
HfC	Hafnium carbide
K_2O	Potassium oxide
MgO	Magnesium oxide
Na_2O	Sodium oxide
O_2	Oxygen
Si_3N_4	Silicon nitride
SiAlON	Silicon aluminate carbide
SiC	Silicon carbide
SiO_2	Silica
SO_3	Sulphur oxide
TaC	Tantalum carbide
Ti-6Al-4V	Alpha-beta titanium alloy
TiO_2	Titania/titanium oxide
ZrB_2	Zirconium diboride
ZrO_2	Zirconia

Symbols List

a	Acceleration	m/s^2
A_e	Nozzle exit area	mm^2
AP	Apparent Porosity	%
ASG	Apparent Specific Gravity	g/cm^3
A_t	Nozzle throat area	mm^2
b	Width	mm
BD	Bulk Density	g/cm^3
d	Thickness	mm
D50	50% of the particles smaller than	µm
D90	90% of the particles smaller than	µm
Dt	Throat diameter	mm
E_{dyn}	Dynamic Elastic Modulus	MN/m^2; MPa
F	Force	N
L	Length	mm
LR	Linear Retraction	%
m	Mass	g
m_o	Empty rocket mass	kg
MoR	Modulus of Rupture	MPa
m_{total}	Mass of rocket loaded with propellants	kg
p_a	Ambient pressure	Pa
p_c	Pressure at nozzle exit	Pa
R_b	Inflection point radius	mm
R_e	Nozzle exit radius	Mm
R_{th}	Throat radius	mm
v_e	Exit gas velocity	m/s
V_{rocket}	Rocket velocity	m/s
W	Weight/Mass	g
WA	Water Absorption	%
α	Diverging angle	º (degrees)
β	Converging angle	º (degrees)
γ	Isentropic exponent	

ε	Strain	MPa
ρ	Density	g/cm^3
σ	Stress	MPa

Chapter 1: Introduction

1.1 Motivation

Rockets enable humanity to broaden its horizons. Although the operating concept of rockets has its beginnings much sooner, it was during the 17th century that the scientific foundations for modern rocketry were laid by Sir Isaac Newton, who developed the famous three scientific laws of physical motion. From there rocketry began to be scientifically studied, with K. Tsiolkovsky proposing in 1898 space exploration by rocket [1], stating that the speed and range of a rocket were only limited by the exhaust velocity of the escaping gases. From there rockets evolved into giant vehicles with the capability of traveling beyond Earth's atmosphere [2] Thus, its operation comes with various challenges, one of them being the choice of the materials used in its components as these must be able to withstand high mechanical and thermal stresses as well as resist oxidation and corrosion caused by the high-velocity exhaust gases.

In its simplest form, a rocket consists of a chamber containing gas under pressure with an opening through which the gas can escape, and in this sense, the apparition of the first recorded use of the rocket engine may be placed in the 13th century, when in a conflict between the Chinese and the Mongols arrows attached with a gunpowder filled "rocket" were used [3]. The gas escaping provides thrust, propelling the rocket in the opposite direction. Nowadays, however, when we think of rockets the image of giant and powerful vehicles capable of carrying heavy loads into orbit and even spacecraft to the moon comes to mind. These rockets burn liquid, solid or hybrid propellants (fuel and oxidizer) creating rapidly expanding and extremely hot gases that are directed through a nozzle creating thrust.

Situated at the end of the rocket engine, the nozzle is composed of two main parts, the narrowest part is called the throat, and just after that is situated the exit cone. The nozzle is used as a way of accelerating the escaping gases by limiting the size of the opening through which these can escape. The nozzle is, therefore, a critical component in the safe operation of a rocket engine as minimal alterations in its profile and geometry lead to losses and alterations in the direction of thrust. The importance of this component coupled with the operating conditions that can reach temperatures exceeding 3000 K and pressure values in the order of 30 MPa [4] while in the presence of supersonic flow speeds, makes material selection a challenging and important study in the design and operation of a rocket engine.

A rocket nozzle, must then, be able to withstand high temperatures with large variations in short amounts of time while in the presence of supersonic flow speeds. This set of operating conditions can lead to a vulnerability to erosion and the formation of cracks and fissures, weakening not only the nozzle but the whole vehicle. To properly protect the nozzle walls from critical failure their thickness may be increased, but at the cost of an unwanted heavier structure, a better solution may then be the development and usage of better suited materials [3]. As such the nozzle

materials need to have good mechanical properties such as high-temperature resistance, good thermal shock resistance, a low expansion coefficient, high melting point, and high thermal conductivity. Historically graphite and carbon-carbon composites have been the preferred materials used to lessen the erosion rate of the nozzle throat, although these materials still fail to maintain proper propulsion due to erosion. As such refractory materials have been studied as possible candidates for noneroding rocket nozzles [5].

Even though refractory ceramics are more widely known and used, there are some metals with the designation of refractory products. Metals such as tungsten, rhenium, niobium, tantalum, and molybdenum are extremely resistant to heat and wear, and have unique mechanical properties with high melting and boiling points, and density. The study of the use of refractory metals on rocket nozzles can, therefore, be of interest.

Ceramic articles are defined as "an article having a glazed or unglazed body of crystalline or partly crystalline structure or of glass, which body is produced from essentially inorganic, non-metallic substances and either is formed and simultaneously or subsequently matured by the action of heat" by the American Society for Testing and Materials (ASTM) [6]. For a material to be considered refractory, it must be able to maintain its pyroscopic resistance above 1500 degrees Celsius (AFNOR standard NF B40-001). As such, refractory ceramics are ceramics capable of maintaining their mechanical properties at high temperatures, making them a worthwhile option to study in a rocket nozzle application. The main constituents of refractory ceramics are usually silica, alumina, and mullite.

1.2 Objectives

During the writing of this dissertation, the main objectives will be to better understand refractory materials, their uses, advantages, and limitations. After the materials are selected, and the mould of the rocket nozzle designed and manufactured, the fabrication process of the ceramic nozzles will be studied. The samples will then be tested to classify the quality of the fabrication process or processes for the different material mixtures.

1.3 Organization

This dissertation will be arranged into several chapters and subdivisions, starting with the state of the art relative to rocket engines and nozzles, followed then by materials and their characteristics. Special attention is given to refractory materials as these will be the principal focus of the study. Chapter 3 relates to study cases, where a few examples of related and relevant articles to this dissertation will be included.

After, the manufacturing procedure of the nozzle samples is presented, including the design in CAD as well as the mould and nozzle fabrication. Finally, the tests and their methodology are presented followed by the results obtained from the analysis.

At the end, there is a conclusion with closing statements and an assessment of the study.

Chapter 2: State of the art

2.1 Rocket Propulsion

2.1.1 Principles of rocket propulsion

As previously mentioned, the scientific study of rocket propulsion is said to have started with the publication of *Philosophiae Naturalis Principia Mathematica* by Sir Isaac Newton in 1687, where nature's physical principles are described among which are three important scientific principles, nowadays known as Newton's Laws of Motion. These laws in their simplest form can be presented as follows:

1. Newton's 1st law states that objects at rest will stay at rest and objects in motion will stay in motion in a straight line unless acted upon by an unbalanced force.
2. Newton's 2nd law gives us that force is equal to mass times acceleration.
3. Newton's 3rd law informs that for every action there is always an opposite and equal reaction.

In the case of a rocket mission, we can determine that as the rocket stands on the launchpad motionless, as the force of gravity is countered by the opposite force of the pad on the rocket, the first law affirms that there needs to be an unbalanced force for it to launch, this force is provided by the thrust created by the rocket engine. The second law (equation 1) determines that the escaping high-speed gases create a force (F) or thrust that increases with mass (m) and acceleration (a):

$$F = m \cdot a \qquad (1)$$

The third law explains that for every action there is an opposite and equal reaction, this law can be observed in a rocket engine as it pushed the gases out of the nozzle (action) the gases push on the rocket (reaction). Combining the second and third laws we observe that the force applied by the rocket on the escaping gases must be equal to that applied by the escaping gases in the rocket, and as such the acceleration of both parts must compensate for the mass discrepancy, which is observed as the rocket starts its climb slow and gradually accelerates as the mass of the propellants is expended. Resuming, following Newton's three laws of motion, we can describe the working principles of a rocket engine as well as predict its behaviour during its operation [7].

It was however in the late 19th century and beginning of the 20th that modern rocketry is said to have been born at the hands of the author of *Study of Outer Space by Rocket Devices,* Tsiolkovsky

who in 1903 published the Tsiolkovsky formula in which the relation between the rocket speed, the gases' speed at the exit and the mass of the rocket and its propellants are established. To this day this equation (equation 2) is the basis for the engineering of spacecraft.

$$V_{rocket} = v_e \ln \frac{m_0}{m_{total}} \qquad (2)$$

Tsiolkovsky also proposed the use of liquid-propellant rockets to achieve a greater range, Robert H. Goddard, who conducted practical experiments with solid-propellant rockets also became convinced that rockets could be better propelled by liquid fuel. The idea of liquid-propellant rockets came with challenges at the time but in 1926 Goddard achieved the first successful liquid-fuel propelled rocket flight. In figure 1 a simple schematic of a what a traditional rocket looks like is presented.

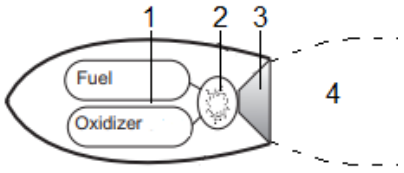

Figure 1. Schematics of a rocket system. 1-propelants storage, 2- combustion chamber, 3- rocket nozzle, 4- plume (altered image from[8]).

2.1.2 Categorization of rocket engines

The rocket has no air intake, both the oxidizer and the fuel are instead carried onboard the vehicle, this makes it a unique kind of propulsive system [8].
Within this special kind of jet propulsion there are different types and categories of rocket engines. There are electric rocket engines that achieve propulsion by consuming electric power (nuclear, solar, batteries, radiation receivers) [9]. Nevertheless, the most commonly used way of grouping rocket engines is into two categories: non-chemical and chemical. Focusing on the latter, we can further categorize them into liquid-propellant, solid-propellant, and hybrid rocket engines.

2.1.2.1 Liquid propellant rocket engines

Liquid-propellant rocket engines, as the name implies, are engines in which the fuel and oxidizer are stored and mixed to achieve combustion in their liquid state and have several advantages that make them the most used type of rocket engine up to date. Advantages such as liquid propellant being found to be more highly energetic, furthermore, carrying fuel and oxidizer in a liquid state allows for the tanks to be lighter weight as the propellants can be stored in a low-pressure chamber making it so that the high pressure necessary to achieve efficient propulsion needs to only be

present in the smaller combustion chamber [10]. Liquid-propellant rockets further lend themselves as the best option for large spacecraft due to their capability to “throttling”, meaning variable thrust levels can be achieved, improving performance in higher altitude conditions, especially in the upper stages of the boosters when manoeuvring is required.
Liquid-propellant rocket engines do, however, also have their shortcomings like the increased complexity of the design due to pump synchronization and accuracy. Rockets that operate at higher levels of thrust also need larger pumps, meaning that the weight of the rocket engine grows significantly. The use of liquid fuel and oxidizer also means that the rocket engine can experience instabilities that lead to variations in pumping rates that in turn create variations in thrust levels that can further aggravate the variations in pumping rates.
The majority of liquid chemical rockets use two separate propellants, the fuel, and the oxidizer. Fuels like kerosene, alcohol, hydrazine (or its derivatives), and liquid nitrogen are frequently used, while nitric acid, nitrogen tetroxide, liquid oxygen, and liquid fluorine are the common oxidizers. Some mixtures of liquid fuel and oxidizer ignite spontaneously upon contact, these are called hypergolic mixtures, the others require an igniter to start combustion being then able to maintain combustion by injecting the propellant into the combustion chamber’s flame [10].

2.1.2.2 Solid propellant rocket engines

On the other hand, solid-propellant rocket engines, more often used in weapon applications, have a simpler design, besides, in its simpler configurations, during runtime propellant burning rate cannot be adjusted, and re-ignition is impossible after extinguishment [11]. The mass on a solid-propellant engine doesn’t vary as much with the exhaust speed as it does on its liquid counterpart as the reinforced structure of the chamber becomes a small part of the total mass for larger rockets. Having a solid-state fuel and oxidizer also means that the propellant has a greater density making the rocket cross-section smaller [12] inducing fewer losses to aerodynamic forces as such the focus of the development of solid-propellant rockets is placed mainly on high-energy, high-density, high-burning-rate propellants.
Traditionally used solid rocket fuels can be divided into two categories, the double-based propellant, which consists of nitrocellulose and nitro-glycerine plus small amounts of additives. In this type of propellant, mostly used in smaller rocket motors, there are no separated fuel and oxidizers. The second type is composite propellants, in this case, the propellant and oxidizer are separate. The oxidizer accounts for about 80% of the total propellant mixture usually ammonium nitrate or chlorate, or potassium chlorate. Normally hydrocarbons are used as fuels.

2.1.2.3 Hybrid rocket engines

In cases where the fuel is in a solid state while the oxidizer is injected in a liquid state, the rocket engine is thus, hybrid. With the appearance of space tourism and new advancements in technologies, hybrid rockets are beginning to see more use. Utilizing solid fuel makes the

production, transportation, and manipulation of the propellant easier and safer. It also simplifies the rocket engine when compared to the use of liquid-propellant as there is no need to synchronize the flows of fuel and oxidizer while maintaining the capability of controlled thrust level by adjusting the flow of only the liquid oxidizer. There are also advantages in the selection of propellants, by using solid fuel there is the option to add metallic powders to increase both density and performance while also achieving the higher energetic levels of the liquid oxidizer.
Hybrid rocket engine shortcomings derive mainly from the need for a large combustion surface for high thrust levels and the combustion apertures needed to achieve it. These apertures can lead to losses of 1% to 2% when compared to the combustion of liquid and solid rocket engines, as well as lead to a lower propellant density. Throughout the combustion process, the diameter of these also varies which in turn changes the oxidizer/fuel ratio and hence the thrust levels as well. In addition, hybrid rocket engines have a slow transient regime during ignition, making the thrust modification during engine speed up low [13].

2.1.2.4 Rocket staging

There are various factors that make the staging of rocket vehicles and its boosters an appealing. Since the ignition of its engines, the tanks that contain the propellants begin to empty, consequently after being completely depleted these boosters hinder the performance of the vehicle by adding unnecessary weight and aerodynamic loads. The commonly used solution is to simply discard of these components once their functions are complete, this process is called staging.
The rocket staging can be divided into serial and parallel, in the first case the stages are stacked, the first, larger, stage is placed under a smaller second stage that fires its engine when the first stage is discarded, this type of staging is used by SpaceX in its falcon 9 rockets. In the case of parallel staging the first stages are added to the sides of a central sustainer rocket, all engines are ignited at launch, however the bigger central sustainer rocket keeps burning after the smaller first stages are discarded of, the space shuttle program used this type of staging to launch the shuttles into orbit [14].
With the operation of a staged vehicle there comes the advantage of being able to use nozzles for smaller altitude variations, which means that the first stage is fitted with a nozzle with exit pressures around one atmosphere and the upper stages with nozzles suited to low pressure environments, usually with much bigger expansion ratios, of around 100 [15].

2.2 Rocket Nozzles

The nozzle represents a large portion of the rocket engine structure, and its geometry largely influences the performance of the engine. A well-designed nozzle will present large gains in performance, especially in areas such as the nozzle contour and its expansion ratio. In search of the optimal nozzle configuration, there has been, intensive research, and development, resulting

in different geometries, being the more well-known, conical, bell, plug, expansion-deflection, and dual bell. The primary objective of a rocket nozzle is to change the characteristics, such as velocity and pressure, of escaping gases flow, in a way that better suits the engine mission. Famously, in 1890, de Laval designed a Convergent-divergent nozzle, capable of increasing a steam jet to a supersonic state. The de Laval nozzle (figure 2) was later applied to a rocket engine.

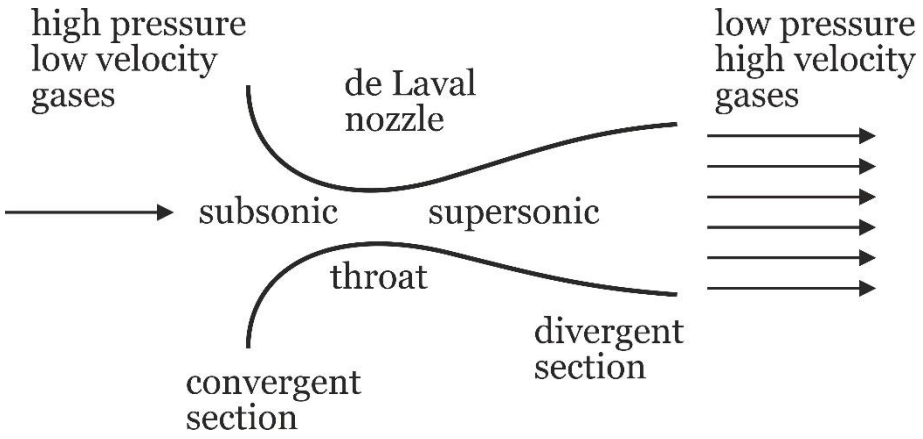

Figure 2. Convergent-divergent nozzle (de Laval nozzle).

A desirable rocket nozzle should be the lightest it can be, have the simplest design possible, and be easy to manufacture while maintaining the maximum performance gains achievable.
Maximum thrust occurs when a parallel uniform flow with the exit pressure, matches the ambient pressure at the exit. The exit area to the throat area of this ideal nozzle can be expressed by equation 3.

$$\frac{A_e}{A_t} = \left(\frac{\gamma-1}{2}\right)^{1/2} \left(\frac{2}{\gamma+1}\right)^{(\gamma+1)/(2(\gamma-1))} \left(\frac{p_a}{p_c}\right)^{-\left(\frac{1}{\gamma}\right)} \left[1 - \left(\frac{p_a}{p_c}\right)^{(\gamma-1)/\gamma}\right]^{-1/2} \qquad (3)$$

A_e/A_t corresponds to the ratio between the exit area and the throat area of the nozzle, while p_a/p_c is the ratio of the ambient and nozzle exit pressure.
γ is the isentropic exponent.
This equation shows us that at higher altitudes the pa/pc ratio, being smaller, means that the expansion ratio will have to be larger [16].

2.2.1 Conical nozzle

The first utilized geometry was the conical nozzle, as it had a very easy manufacturing process. The conical nozzle with a 15° diverging angle can produce a thrust coefficient only 1.7% smaller than the ideal nozzle and it changes little with altitude [16]. The conical nozzle tends to be heavier and longer than more modern and complex designs, its losses also occur at lower altitudes. The conical nozzle (figure 3) length and performance still serve as a benchmark for new designs.
The conical nozzles are its straight walls from throat to exit, as well as the incomplete flow turning.

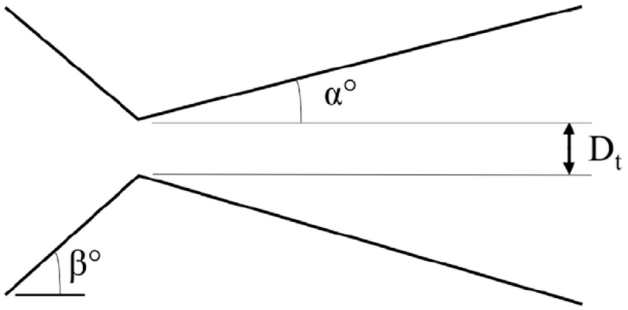

Figure 3. Conical nozzle. (D_t: diameter of the throat; α: diverging angle; β: converging angle) [17].

2.2.2 Bell nozzle

The bell is the most common type of rocket engine nozzle geometry. This concept allows a steep angle in the section immediately after the throat, as the pressure is high enough that separation won't occur, the wall contour is then gradually reversed until a low divergence angle is attained at the nozzle exit. As such, this geometry allows for shorter nozzles when compared to the conical design, around 20% [16].
The efficiency of the bell nozzle can diminish at low altitudes because of over-expansion and be improved at higher altitudes through under-expansion. At altitudes above those the nozzle was optimized to, as a result of the lower atmospheric pressure, the exhaust flow expands past the nozzle wall, meaning that there is no reaction force being exerted on the nozzle wall by this over-expanded part of the exhaust plume, thus decreased thrust and lower efficiency [18].
Losses in thrust can be lessened by adjusting the wall contour at the nozzle exit, making the flow escape in a direction closer to the axial.
There are different contours of the bell geometry each of them with different flow characteristics on the finished nozzle. Truncated ideal contour bell nozzles tend to be longer with a less steep angle after the throat section, having the walls transition to nearly straight at the exit, practically complete flow turning is achieved. Thrust optimized contour has a sharper transition from the high angle after the throat to the near straight wall at the exit, it maintains the virtually complete

flow turning. Thrust optimized parabola consists of a parabolic approximation of the truncated ideal contour (figure 4), leading to a higher wall pressure at the exit of the nozzle, contributing to a smaller risk of the occurrence of side loads.

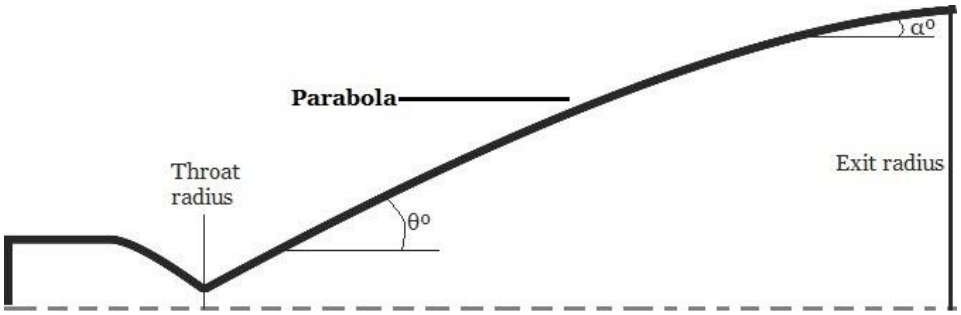

Figure 4. Bell nozzle profile (θ: initial divergence angle; α: smaller divergence angle at the exit). Altered from [19].

2.2.3 Aerospike/Plug nozzle

The plug nozzle is considered an advanced geometry. These nozzles are composed of a semi-conventional design primary nozzle, with a plug that helps with external expansion. The term plug nozzle is usually used in reference to two types of nozzles, the full-length spike, aerospike, or the shortened conical, plug nozzle.

This geometry allows, through its interaction with the external ambient, to delay and avoid the flow separation that plagues bell-type nozzles. The plug nozzle is also resistant to altitude changes, as the boundary layer flow works as a nozzle wall, allowing the nozzle to compensate for the variations in ambient pressure by expanding to match it.

While operating at a nozzle pressure ratio below the one the nozzle was projected to, the boundary layer is forced nearer the plug by naturally occurring compression and expansion waves trying to match the ambient pressure. While at equal or higher nozzle pressure ratios it operates as a more traditional Convergent-divergent nozzle. So, the plug nozzle design (figure 5), allows, the escaping gases, to expand gradually and smoothly from the high pressures at the combustion chamber exit to the lower ambient pressures so that the flow is uniform and parallel to the nozzle axle at the exit [16].

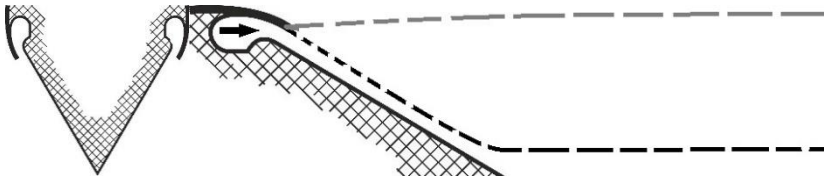

Figure 5. Aerospike nozzle and its operation. The darker dotted line represents the escape flow as the surrounding pressure is higher than that of the flow, the lighter line represents the flow at the ideal ambient pressure, where the flow direction is the same as the nozzle axis.

2.2.4 Dual-Bell nozzle

The bell nozzle geometry has the disadvantage that it is unoptimizable for different operating altitudes, resulting from this, the dual-bell nozzle appears, in 1949, as a means of being able to have a geometry capable of auto-adaptation of the flow, in other words, this allows the nozzle to be better suited for operation both in low and high altitudes, instead of having to find a compromise in between.

Dual-bell nozzles are based on being able to force flow separation on a desired, inflection, point, thus allowing the nozzle to have increased performance at low altitudes, controlled and symmetrical separation of the flow also ensures that the production of loads is limited. As the altitude rises the flow expands until it attaches to the higher angle nozzle wall, resulting in an increase in thrust [20].

This design was found to have better overall performance than that of the traditional bell geometry, with the atmospheric pressure restricting the expansion of the exhaust flow at lower altitudes, the efficiency of the altitude adaptive design of the dual-bell nozzle (figure 6) is considerably higher. In fact, at low altitudes, the fuel savings were measured to be around 25-30% in comparison with the single bell design. At higher altitudes, the exhaust flow expands, as previously mentioned, to a larger effective nozzle area ratio.

These factors combined make the dual-bell nozzle SSTO (Single Stage to Orbit) flight capable [21].

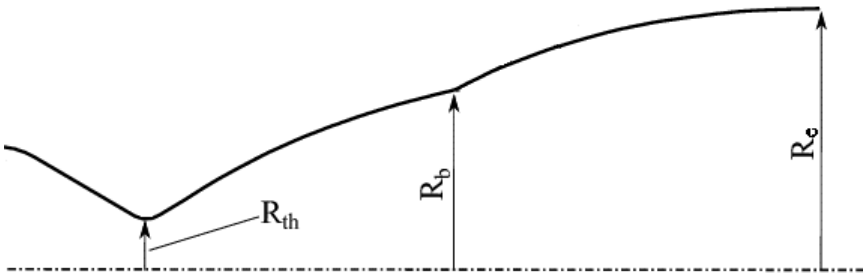

Figure 6. Dual bell nozzle profile. R_{th}: Throat radius, R_b: Inflection point radius, R_e: Nozzle exit radius [19].

2.2.5 Other types of nozzles

There are less well-known and used designs, such as the expansion-deflexion, and the multigrid nozzles. Although the previously given designs are the more commonly known, the research and development of more efficient and overall better-suited geometries continue. The table 1 shows us the main advantages and disadvantages of the various types of nozzles [16].

Nozzle Type	Advantages	Disadvantages
Conical	Easier manufacturing and optimization Simpler design Continuous angle (Compromise between divergence angle and nozzle length)	Flow not completely axial at exit Longer than bell nozzle (Compromise between divergence angle and nozzle length) Unoptimized pressure thrust at different altitudes
Bell	Shorter in size than the conical nozzle Better performing than the conical nozzle	Complex manufacturing Difficult to be optimized and unoptimizable to different altitudes
Aerospike/Plug	Better flow separation resistance Quieter and smaller in size Suited to optimization at different altitudes	Challenging colling of the central plug
Dual-Bell	Controlled flow separation at low altitudes, thus limits strong side loads. Able to operate at both low and high altitudes. Thus, SSTO flight capable.	High side loads at the moment of transitioning between operating modes. Higher manufacturing and designing difficulty

Table 1. Different nozzle geometries and characteristics.

It should be mentioned that there are, obviously, more types and variations of nozzle designs that are not mentioned, either in the previous text or table, although the study of these can be riveting, in this case, the complexity of the nozzle is desired to be simple and of easy manufacturing, as such only, the four more well-known geometries were considered.

2.3 Materials

2.3.1 Differentiating Materials

There is an enormous number of materials each one with its characteristics, as such, there are ways to group together materials based on various parameters, as a way of facilitating the search for the ones that may have the desired set of attributes.

The nozzle of a rocket engine is an area of extremes, being exposed to high temperatures, pressures, and velocities. In the aerospace industry, the use of a material with specifications that do not meet the requisites necessary can lead to extensive damage or even the total loss of vehicles and objects with very high costs, or even loss of life. Therefore, the materials used in the nozzle must be carefully considered and studied.

Materials have various quantifiable properties. Strength, elasticity module, density, and fusion temperature are some of the many properties that help us know how materials will react to certain situations, thus making it possible to make an informed decision on the materials to use.

2.3.1.1 Properties of materials

Mechanical properties

Some common properties to evaluate materials are:

- Density or specific volume (kg/m^3; m^3/kg):

$$Density = \frac{mass}{Volume}\left(\frac{kg}{m^3}\right); Specific\ Volume: \frac{Volume}{mass}\left(\frac{m^3}{kg}\right) \quad (4)$$

Density is the mass per volume unit of a material while the specific volume is the opposite (volume per mass unit). In a spacecraft is very important to maintain the weight to a minimum as the cost and complexity of launching missions to space only increases with weight. As such it is useful to pay attention to the density of the chosen materials.

- Mechanical Strength (MPa):

Materials strength measures the capacity it has to resist deformation, and the ability to support a load without breaking. This can be displayed in a stress/strain graphic (figure 7) where it is possible to identify the yield (point of transition from elastic to plastic regime) and tensile (rupture point) strength of the material.

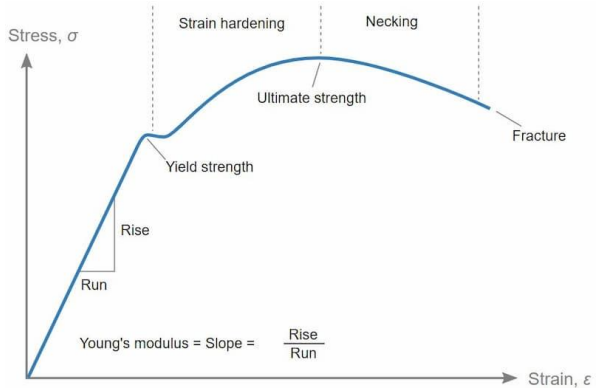

Figure 7. Example of a material strength graphic [22].

- Specific fatigue strength (MPa):

As the name suggests this property evaluates the resistance a material has to failure after various cycles of being subject to forces. In other words, is the highest stress that the material can sustain, without breaking, after a determined number of cycles. It is important to note that besides the stress, amplitude and frequency also influence this property. The fatigue strength of a material is usually presented either in the form of a graphic (figure 8) or in MPa for a predetermined number of cycles (usually between 10^8 and 5 x 10^8).

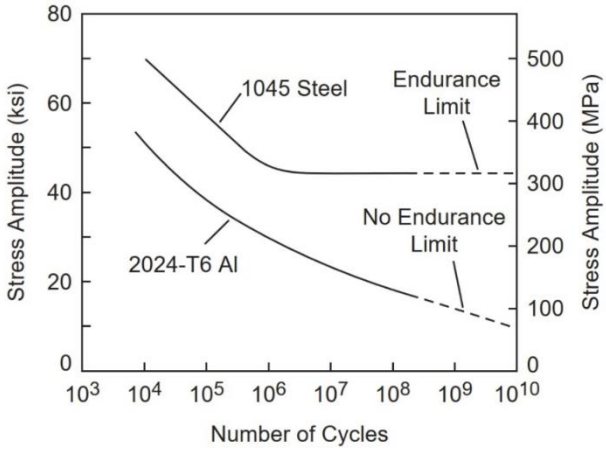

Figure 8. Example fatigue strength graphic of low-carbon steel. S-N curve (strength versus the number of cycles) [23].

- Hardness and Toughness (GPa):

A material's hardness measures its resistance to localized plastic deformation, i.e., the ability to resist abrasion, penetration, and plastic deformation, like small dents or scratches. Its toughness can have different meanings. Fracture toughness is the resistance it has to fracture, in particular when a crack or other type of defect is present. Additionally, toughness can be defined as the capacity the material has to absorb energy and plastically deform before fracturing. Temperature severely affects the toughness and hardness of most materials, as well as other properties. There are various ways of testing and measuring the hardness and toughness of a material, including the Brinell, Rockwell, and Knoop hardness tests.

- Ductility (dimensionless quantity):

Ductility is a property that indicates its capacity to be stretched, folded, or plastically deformed without fracturing. Ductility is required so that metals can be easily formed into various shapes, making ductile metals like aluminium desirable and extensively used in the aeronautical industry. Ductile materials are distinct from malleable ones, as malleability is the aptitude of metal, mainly in sheets, to be hammered, laminated, or pressed without fracturing. Ductility measures are taken from the amount of permanent deformation indicated by the stress-strain curve.

- Elasticity (Pa):

A material that is capable of returning to its original size and form after the stress that made it deform is removed is said to be an elastic material. The elasticity modulus corresponds to the ratio of stress, below the proportional limit, to its parallel strain, and it's used as a way of comparing the elasticity of different materials [24].

Thermal properties

- Fusion temperature (K):

The temperature at which a material reaches its liquid state by means of heat.

- Thermal conductivity (W/mK):

Thermal conductivity is a property of a material that relates to its resistance, or lack of it, to transfer heat within itself.

- Coefficient of thermal expansion (K^{-1}):

The amount of expansion and contraction a material suffers under thermal load (heat or cooling). This property is especially relevant when there are different materials connected or in contact as different coefficients of thermal expansion can lead to unwanted and damaging stresses being introduced in either of the materials.

These mechanical and thermal properties of materials are established by performing laboratory experiments that replicate, the service conditions the material will encounter, as nearly as possible.

It is important to reiterate that measured material properties are not exact quantities, as even the most precise measurement devices and controlled tests have variability in the collected data.

As previously stated, there are various types of materials, each with its advantages and disadvantages and each suited to specific situations.

2.3.1.2 Polymers

Polymers are macromolecules formed from smaller units called monomers that repeat forming a long chain. Polymers have a wide range of applications like construction material, textile fibres, and even microelectronics processing.

Even though polymers are easy and cheap to manufacture, their mechanical strength and service temperatures are low relative to metals and ceramics, preventing them from being an option to use in environments such as the ones a rocket nozzle might be subjected to. Some polymers like PEEK (polyether ether ketone) are engineered to have great heat resistance in relation to more traditional types of polymers. Still, PEEK melting point is 390 ºC (663 K) [25]. The use of polymers in the context of rocket nozzles isn't an alternative as temperatures, even at the rocket nozzle exit, depending on the propellants, reach temperatures superior to 2000 K [26].

Still, polymers are useful to the aeronautical industry, and found in great quantities in places such as the cockpit, valves and wiring and cable coatings, among many others.

Polyimides are a class of polymers that are prominent in the aerospace industry, due to their wear, chemical, radiation and temperature resistance. These materials can be found in applications such as engine housings and electronic packaging, along with other non-loading structural contexts. Polyimides are used in aircrafts, weapon systems and space vehicles, due to their preservation of mechanical properties at high temperatures, because of their thermal stability, and solvent and chemical resistance [27].

2.3.1.3 Metals

Metals, chemically, are any of the elements that have a positive electrical charge. As a material, metals are composed of one or more metallic elements, and often also non-metallic elements in small quantities.

Metals are quite stiff and strong, but still ductile and resistant to fracture. These characteristics make metals a staple in structural applications. These materials are also notably good conductors of electricity and heat and usually have a polished surface appearance. Some also have desirable magnetic properties.

In the aeronautical and aerospace industry, metals and metal alloys are especially popular, thanks to their low density, hence low weight, easiness of manufacturing and processing, and reasonably low cost. Aluminium, titanium, and steel are extensively used in the construction of aircraft, notably in structural components like the wings, fuselage, and landing gear. As an example, in the Boeing 747, the weight percentage of these materials is 81%, 4%, and 13% respectively, totalling 98% of the total weight.

Some of the metals and alloys used in the aeronautical and aerospace industries are presented in table 2:

Boeing Airplanes	*Aluminium Alloys*	*Titanium Alloys*	*Steels*	*Composites*	*Others*
747	81	4	13	1	1
757	78	6	12	3	1
767	80	2	14	3	1
777	70	7	11	11	1
787	20	15	10	50	5

Table 2. Presence in percentage of metals in commercial aircrafts [24].

Rocket nozzles are also often made of metallic alloys. Titanium, tungsten, and aluminium are some of the frequently used metals on nozzles. Ti-6Al-4V is a commonly used material because of its high strength and high tolerance to temperature variations [28]. There are also refractory metal alloys composed of Vanadium, Niobium, Molybdenum, and Tungsten with extraordinary high-temperature properties, these however have challenging fabrication and machining processes as well as high costs associated. Degradation due to oxidation and corrosion also present challenges to the use of refractory metallic alloys.

2.3.1.4 Ceramics

Ceramics are inorganic and non-metallic materials, most of them being compounds among metallic and non-metallic elements in which the bonds between atoms are predominantly or totally ionic having some covalent character.

Though the meaning of the term ceramic is not simple to define, the concept is historically connected to pottery, and thus to the use of clay soils [29]. The clay mixed with water forms a paste that can be moulded. But it is the “cooking” or firing of the clay-water mixture that makes it a ceramic, as the water must be permanently removed. It is because of the firing that physicochemical alterations occur making the material no longer plastic or capable of rehydration.

After substantial progress in material science, ceramics have evolved into a new generation of material. Today’s ceramics, are used in electronics, aircraft, spacecraft, and many other applications are a new and evolved generation from the traditional clay-based ceramics like porcelain, bricks, and tiles.

Composed of at least two elements the crystal structures of ceramics are often more complex than those of metals. The two, ceramics and metals, are inherently different and as such, tend to have completely distinct, and even complementing, applications.

Ceramics can be divided into a classification based on the application that groups them into glasses, clay products, abrasives, cement, advanced ceramics, and refractories.

The applications of these can range from oven windows in the case of glass-ceramics, to building bricks for clay products, to grinding wheels made of abrasive ceramics, to the use of refractory ceramics in furnace linings, and general high temperature, severe environments [30].

2.3.1.5 Composites

Composite materials are the result of the union of two or more, different in nature, materials with their final properties being as a whole greater than those of the constituent materials by themselves. Composites unite two materials of different phases, a matrix, and a reinforcement, in which the goal is that the final material has better properties than those of the matrix and reinforcer alone. The more common types of composites are the ones with polymeric matrixes reinforced with fibres like fibre-glass, carbon-fibre, and Kevlar, their light weight, good mechanical resistance, and durability are very much appreciated, especially in the car and aeronautical industries. Although the initial cost may be relatively high, with the repetition of the manufacturing of the same parts, the price per part decreases making composite prices competitive in the long term.

There are three different classes of composite materials, MMC (metal matrix composite), CMC (ceramic matrix composite), and PMC (polymer matrix composite).

Considering that single-phase materials tend to have low resistances pertaining to fracture toughness, and thermal shock, the utilization of composites can be made to improve such shortcomings. In the case of ceramics submitted to harsh applications such as rocket propulsion, the utilization of ultra-high temperature ceramics (UHTCs) composites with silicon-based ceramic be it in the form of particles or fibres, showed the resulting composite to have a significantly better response to thermal shock when exposed to aggressive chemical environments [31].

Carbon, and carbon/carbon composites, because of their low density, low coefficient of thermal expansion, high specific strength, and retention of mechanical properties at high temperatures [32], are emerging as one of possible solutions of materials to replace the more traditional metal alloys used in the construction of rocket nozzles, however research is still essential due to the ablation the throat of C/C nozzles has been found to suffer from.

2.3.2 Materials applied to the aerospace and aeronautical industries

2.3.2.1 Polymer applications

Polymer's ability to have relatively low weight (20 – 40% savings), being corrosion resistant to most chemicals and a long durability, while being able to be designed to have a relative high strength, has made these materials an excellent selection to various applications in the aeronautical and especially the aerospace industry. Solar sails, antennas, sunshields, rovers are among the structures that require flexible and compliant materials that may be folded for small volume transportation and then deployed in space into large lightweight structures, furthermore cockpit and crew gear, and optical instruments are also mainly made from polymers [33].

2.3.2.2 Metal and metal alloys applications

In the current state of the industry, and because of their high-strength and stability at high temperatures, gas turbines are led by the utilization of nickel-based superalloys, and the technological advancements have been instead in design changes, with the development of cooled and blades with a TBC (Thermal Barrier Coating). In the case of high-bypass engines, alloys of titanium and nickel-based superalloys are usually used in the exhaust nozzles.
Since the replacement of wood by aluminium alloys (table 3), these have been the main airframe material, and even though the increase in composite materials means the decrease in the utilization of aluminium alloys, it is expected that high-strength aluminium alloys will stay relevant materials in the aeronautical industry, as a result of the relatively high-strength and low cost, lightweight, and ease of fabrication inherent to the aluminium alloys [34].

Product	Strength level	Application
Sheet	Damage Tolerant	Fuselage/pressure cabin skins
Plate	Damage Tolerant	Lower wing cover
	Medium	Tactical aircraft fuselage panels
	Medium	Tactical aircraft bulkhead
	Medium	Internal fuselage structures
	High	Upper wing cover
	Medium	Spars, ribs, internal structures
Forgings	High	Wing/Fuselage attachments
Extrusions	Damage tolerant	Lower wing stringers, fuselage/pressure cabin stringers
	Medium/High	Fuselage stringers and frames, upper wing stringers, floor beams, seat rails

Table 3. Aluminium alloys applications in airframe structures [34].

Titanium alloys can be often used in the compressor blades and disks of the turbofan engines, as well as in anti-icing and engine bypass ducts, the landing gear structure, helicopter rotor heads among others.

2.3.2.3 Ceramics applications

The aerospace industry that can profit from the utilization of ceramic material technologies, thermal protection systems, hot primary structures and propulsion and exhaust washed structures.

A TPS (Thermal Protection System) consists of a system designed to protect and insulate the vehicle from the aerothermal stresses. The main and most well-known example is that of the ceramic tiles used in the Space Shuttle Orbiter. These ceramic tiles with a glass-based coating permitted a consistent aerodynamic performance from the lifting-body geometry of the Space Shuttle by being volumetrically and geometrically stable. These ceramic tiles had a low density that allow the TPS to be relatively lightweight, however the low impact resistance and strength oxidation of the tiles led to a sever maintenance burden after each re-entry.

TBCs (Thermal Barrier Coatings) contribute to the improved efficiencies and thrust values of engines and gas turbines. The thermal insulating properties of the TBCs can help improve the temperature limits of the engine blades and disks [35].

However, nowadays the focus of the integration of ceramics in the aerospace and aeronautical industries has been mainly focused on the development of hypersonic flight.

In hypersonic capable aircrafts, structures like the leading edges and nose cone reach high temperatures. In the SR-71 Blackbird titanium structures were used to enable flight at speeds above Mach 3, however for higher Mach numbers ceramics are likely the better suited materials for airframes or thermal protection systems. UHTCs are seen as a promising class of materials for application in leading edges of hypersonic vehicles. Refractory in nature, carbides, nitrides, and borides, are appealing to be applied in the higher heat load areas. The hypersonic demonstrator vehicle X-43 utilizes ceramic based materials in the nose leading edge [36].

However, and due to challenges associated with the impact resistance and brittleness at lower temperatures of ceramics the interest has been shifting from high temperature ceramics to CMCs.

2.3.2.4 Composites applications

As it's already been established, structural materials for the aeronautical industry must be mechanically capable and durable, as well as lightweight. The previously discussed aluminium alloys have been at the forefront of aircraft manufacturing for nearly a century.

However newer models, like the modern Airbus A350 or Boeing 787 (figure 9), have been adopting CFRP (carbon fibre reinforced polymers) as an alternative to the commonly used aluminium (table 3). These materials, in addition to their comparative advantages and disadvantages, are nevertheless costlier which has led to doubts regarding their utilization in more conventional and smaller aircrafts. Thus, for the foreseeable future the better option for the fabrication of airframe structures is seen as being a hybrid of metallic alloys and composites.

When comparing CFRPs to aluminium alloys, the composites have significantly higher specific stiffnesses, greater flexibility when designing structurally efficient components, due to their

tailored directional properties. Furthermore, around 20% weight savings can be achieved, contributing to a more fuel-efficient aircraft, CFRPs also have better dimensional stability, improved fatigue strength and in some cases vibration damping [34].

Aluminium alloys are cheaper both in material and labour costs. CFRPs also are susceptible to have fabrication related flaws. Composite components also have higher susceptibility to impact damage, lower electrical conductivity and are sensitive to moisture pick-up. Non-destructive inspections are also harder with CFRPs. Besides, composites in the presence of aluminium suffer from galvanic corrosion which leads to the necessity for isolation.

Composites in the aerospace and aeronautical industry are still in an early stage, thus it is to be expected big strides in the utilization of such materials in the future [37].

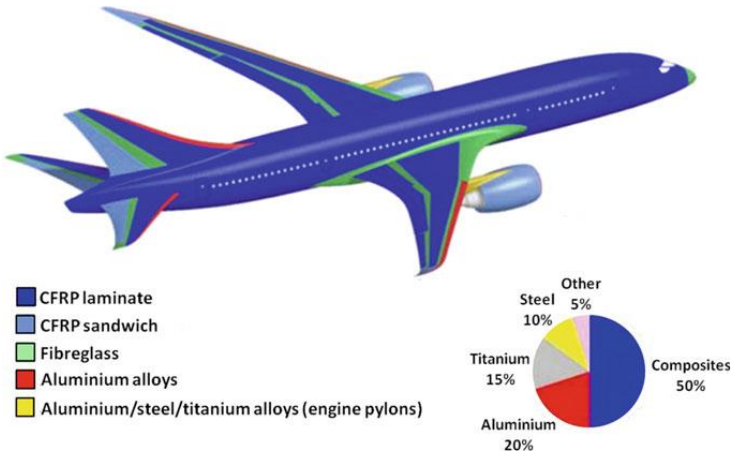

Figure 9. Materials distribution and percentage in the Boeing 787 aircraft [34].

Composite is a term that encompasses a great variety of materials. As previously discussed, a composite can have different matrix materials (PMC, CMC, MMC). Carbon/Carbon composites may be one of the most famous composites utilizations in the aerospace industry due to their application in the Space Shuttle program.

C/C composites have high thermal stability, specific strength, stiffness, fracture toughness and thermal conductivity while having a low coefficient of thermal expansion, properties that make them appealing to applications as TPSs. C/C composites also are less dense than some of the traditional metals and alloys.

C/C composites are also found in the aircraft break disks, rocket nozzles and nozzle throats and sometimes in combustion chambers. Besides C/C, there are also C/SiC composites, these are often considered for application in environments where a longer life span and thus better response to corrosion and erosion is needed than that presented by the C/C composites, applications such as jet engine vanes, TPSs, combustion chambers and studies are being conducted as to their utilization in rocket nozzle throats [34].

2.3.2.5 Nozzle materials

Materials available and tested for the construction of rocket nozzles range from refractory metals and metal carbides, graphite, ceramics, composites such as carbon/carbon, and fibre-reinforced plastics.

There are options better suited for each desired situation, thus the choice of material must derive from the characteristics of the environment where the material will be applied, as each category of materials may show significantly superior performance under the right application. Graphite nozzles may perform when applied to rockets where the least oxidizing propellants are used, however, these nozzles are usually severely eroded and must consequently be replaced after a single mission. Therefore, while graphite is a valuable material for nozzle applications under propellants with low oxidation environments and for single-use rockets, fully densified refractory-metals nozzles may be a better option to cases where more erosion resistance and resistance to cracking under thermal shock are needed. Regarding ceramics, research into UHTCs, like zirconium, and hafnium diborides or carbides have also grown in popularity in the rocketry field thanks to their higher melting points, and high-temperature strength as well as the oxidation strength for temperatures greater than 2300 K [38].

2.3.3 Refractory Ceramic Materials

Refractory comes from the Latin *"Refratarius"* meaning resistant, that refuses to subjugate, on the other hand, when applied to materials, refractory means resistance to high temperatures. For a material to be considered refractory it must resist, implying that it maintains its physical properties and structural integrity, above a predetermined point. According to AFNOR standard NF B 40-001: "Refractory materials are materials and products other than metals and alloys (without excluding those containing a metal constituent), whose pyroscopic resistance is equivalent to at least 1500 ºC" [39].

Pyroscopic resistance of a material is the temperature at which the product, exposed to a gradual rise in temperature under standard conditions, softens and sags under its own weight.

Refractory materials' main characteristics are their ability to withstand high temperatures and their infusibility, and their basic functions are to ensure the physical safety of personnel and structures between the interior hot material and the outer shell.

There are various ways of classifying the sizeable variety of refractory materials, the four principal methods are chemical and mineralogic nature, density, form, and manufacturing technology and can be seen in table 4.

Method of classification	Classification	Examples/Characteristics
Chemical and mineralogic nature	Acid refractories	Silica-alumina family.
	Basic refractories	Magnesia, dolomite, chromite.
	Special refractories	Carbon, carbides, nitrides, spinels, zirconia, etc.
Density	Dense products	Under 45% porosity.
	Light products	Heat insulating materials, over 45% porosity.
Form	Shaped products	Appear in the final form they will be used. Bricks or special shapes.
	Unshaped products	Made of castable, ramming materials, cement, mortars, pastes, plastics, and coatings. Usually, consist of pulverulent mixtures delivered in bags or barrels and which thus require shaping before usage
	Semi-rigid products.	Products shaped separately can be deformed during processing. Generally referring to the fibre-based ceramic materials delivered in the form of plates or panels.
Manufacturing technology	Fusion of raw materials	Allowing the production of electrofused blocks or special shapes.
	Transformation of a pulverulent made up of non-cohesive particles into a consolidated material	Sintering or chemical reaction leads to the cohesion of the refractory material, with the utilization of a binder. Shaping is a result of varied processes.

Table 4. Classifications of refractory materials.

The various processes that lead to the shaping of the material manufactured through the transformation of pulverulent made up of non-cohesive particles include dry pressing, vacuum extrusion, injection moulding, isostatic pressing, casting/vibrating, or gunning.

2.3.3.1 Properties of refractory materials

It has been previously discussed, in the 2.3.1 point, the different properties of materials and the importance these characteristics play in the decision-making process of the application of the better suited material.

When studying refractory materials there are properties that require especial attention in the manufacturing and quality control processes as these characteristics are particularly important in the applications the refractory products are subjected to.

Melting point/temperature

The melting point of refractory materials (table 5) describes the temperature at which chemical changes start to happen, thus, the melting point of a refractory product reflects its ability to withstand high temperatures.

Compounds	Melting Points (ºC)
MgO (pure sintered)	2800
CaO	2571
SiC (pure)	2249
MgO (90-95%)	2193
Cr_2O_3	2138
Al_2O_3 (pure sintered)	2050
Fireclay	1871
SiO_2	1715
Kaolin	1816
Chromite	2182
Titania	1849

Table 5. Melting points of compounds used in the manufacturing of refractory products [40].

Porosity and slag permeability

The porosity of a material reveals the open pore space of it. These spaces are propense to be infiltrated by slag, molten metal and gases which can in time lead to the degradation of the material. The decrease in porosity of the material incresases its strength and thermal conductivity, thus materials with high porosity are better insulators while those with low porosity have better mechanical and slag resistance. The porosity of a material is presented in a percentage of open pore space in its overall volume.

Density

As already stated, the density of a material is a ratio of weight and volume. The porosity and density of refractory materials are often entangled as a product with lower porosity will have a higher overall density. Hence, the density, not unlike the porosity, is connected to the materials ability to resist heat and slag penetration, as well as its volume stability.

Refractoriness/ Pyrometric cone equivalent

The refractoriness of a material is specified by its PCE (pyrometric cone equivalent) which is a test of the temperature, and time, at which the material starts to deform under its own load.
For refractory products, however, in most cases the RUL (refractoriness and load) is more important that the PCE.

Refractoriness under load (RUL)

The RUL test is made under service conditions, both in terms of temperature and load, helping to understand the point at which the refractory product may collapse or suffer damage. It is notable that during actual service the product may only be partially exposed to the high temperatures, allowing the cooler portion of the material to withstand some, if not most, of the load.

Creep

The creep of a material is a property that relates to the deformation it suffers at a given temperature in a predetermined time window under stress. A 0,3% deformation after 50 hours is a figure that is considered to represent, in standard load and temperature working conditions, that the refractory meets the criteria of acceptance.

Thermal expansion/ Volume stability

Refractory materials are utilized in high temperature application, as such and due to the environments, the refractory materials are subjected to, the material may expand or shrink which can be damaging not only to the material itself but also to the structure it is applied to. The Permanent Linear Change (PLC) on the reheating and cooling of materials is a percentage between the increase or decrease in length and/or volume of the material and its original volume that quantifies the volume stability of the material.

Spalling

A refractory material might suffer from the occurrence of fractures or spalling. Spalling can be caused by an abrupt change in temperature of the material, a difference in thermal expansion coefficients of the surface layer and the body of the brick, slag penetration, among other occurrences.

Thermal conductivity

The quantity of heat transferred, in a determined time, through a unit area in a direction standard to the surface of the material is called thermal conductivity. Depending on the desired application, a refractory product may be required to have a high or a low thermal conductivity. As already mentioned, the porosity is a major contributor to the heat transferring capabilities of the material [40]–[42].

2.3.3.2 Formation of refractory materials

The formation of a cohesive particle refractory product starts with the aggregates (one or more minerals), to which is being added additives that provide or strengthen specific characteristics, then a binding agent is used to ensure the cohesion of the product, resulting in a final product that is porous which contributes to some properties as well.

Aggregates (tables 6 and 7) are typically made up of one or more minerals, that impart the main qualities to the finish product. These minerals are mostly oxides in an amorphous or crystalline form and constitute from 70% to 100% of the final composition. The raw materials can be either natural, requiring processing due to impurities, or synthetic with very high levels of purity, transformed from natural raw materials or by physicochemical reactions from synthetic products.

Group	Raw Material	Type	Chemical composition	
SILICA-ALUMINA SYSTEM			Al2O3	SiO_2
Alumina	Tabular alumina	Synthetic	99	
	Calcinated alumina	Synthetic	99	
	White electrofused alumina	Synthetic	99	
	Brown electrofused alumina	Synthetic	94-96	
	Refractory bauxite	Natural	82-89	
	Sintered and electrofused mullite	Synthetic	72-78	
	Kyanite	Natural	55-59	
	Andalusite	Natural	52-59	
Silica-Alumina	Clay chamottes	Natural	35-60	
	Refractory clays	Natural	30-45	
	Bentonite-pyrophyllites	Natural	20-35	
	Perlite-vermiculite	Natural	9-12	40-75
Silica	Quartzites	Natural		99
	Vitreous silica	Natural		99
	Volatile silica	Synthetic		90-95

Table 6. Main aggregates of the silica-alumina system and their characteristics (modified from [30]).

BASIC			MgO	CaO	SiO2	Cr2O3	Al2O3
Magnesia	Electrofused magnesia	Synthetic	93-99				
	Natural magnesia	Synthetic	70-97	2-20			
Forsterite	Olivine	Natural	39-44		41-50		
Dolomite	Sintered dolomite	Synthetic	38	59			
Spinel	Electrofused spinel	Synthetic	28-31				67-72
	Sintered spinel	Synthetic	10-28				67-90
Chrome	Chromite	Natural	16-20			32-45	15-28
	Co-clinker magnesia/chromite	Synthetic	55-60			15-20	
	Chrome oxide green	Synthetic				99	
OTHERS			**C**		**SiC**	**ZrO_2**	**Al_2O_3**
Carbon	Graphite	Natural	77-98				
	Carbon black	Synthetic	99				
Carbide	Silicon carbide	Synthetic			87-99		
Zirconium	Zircon sand	Natural				64-67	
	Dense zirconia	Synthetic				80-95	
	Electrofused zirconia/mullite	Synthetic				35-37	46-52

Table 7. Main basic aggregates and others and their characteristics (modified from [29]).

Binding systems (table 8), although not refractory themselves, are essential as they ensure the permanent cohesion of all the elements that make the refractory products. There are four groups into which the binding systems can be divided.

Ceramic bond, where the physical and mineralogic structure of the finer part of the materials is assigned by ceramization reactions, is usually used in high-temperature situations.

Hydraulic bond is a cold binding method as the binding comes from the hydration of an aluminous refractory cement, consisting of a calcium aluminates mixture, that is added to the product at low temperatures. A typical binder for castable refractory, irrespective of its contents, is around 30% (high), around 2% to 10% (low), and less than 2% (ultra-low).

Mineral chemical bonds react in a complex manner, either by a direct chemical reaction with the finer part of the aggregate or by the formation of a gel that changes its specific structure at low temperatures. These types of binders also are not very refractory, so their concentration is generally less than 5%.

Organic chemical bonds are referred to as low or average temperature bonds, the hardening process involves polymerization for resins or polycondensation and cross-linking for pitch and tar. As the temperature rises, these types of binders leave behind residual carbon in the porosity which improves the corrosion resistance of the final product.

Type of bond	Binder	Type of products
Ceramic	Clay	Shaped and Unshaped
	Pulverulent oxides	Shaped and Unshaped
	Mullite, Si3N4, SiAlON, AlN	Shaped and Unshaped
Mineral chemical	Sodium silicate	Unshaped
	Silica gel	Shaped
	Ethyle silicate	Shaped
	Phosphoric acid	Shaped
	Sodium, aluminium phosphates	Shaped and Unshaped
	Boric acid	Shaped and Unshaped
Organic	Cellulose derivatives	Shaped and Unshaped
	Tar, pitch	Shaped and Unshaped
Hydraulic	Aluminous cements	Unshaped

Table 8. Types of bond and main binders [29].

The **additive's** (table 9) purpose is to, as the name suggests, add and/or reinforce desired characteristics to the refractory product.

ADDITIVES	ADDED PROPERTIES
Chromite	Increase in the refractoriness
Sintered and eletrofused mullite	
Spinel	
Aluminium (mean temperature)	Increase in hot mechanical strength
Silicon metal (high temperatures) + carbon	
Silicon carbide	Increase in the corrosion resistance
Graphite chromium oxide	
Zirconia	
Spinel	
Carbon black, pitch, resin	
Silicon carbide	Increase in the resistance to abrasion and erosion
Electrofused alumina	
Mullite	Increase in the resistance to thermal shocks
Graphite	
Vitreous silica	
Silicon carbide	Increases thermal conductivity
Graphite	
Pyrolisable products (creation of porosity)	Decrease in thermal conductivity
Impregnation by pitch and tar	Increases compactness (less porosity)
Clay (shrinkage)	Permanent change
Kyanite, quartz sand (expansion)	
Plasticizers: Clay, bentonite, various organic products	Rheological Modifications
Deflocculants, dispersants: Miscellaneous organic products	

Table 9. Additives and the properties they add [29].

Some common finished refractory products are fireclay, high-alumina fireclay, silica, periclase, and periclase-chrome ore.

2.3.3.3 Characteristics of some refractory products

A finished refractory product is not only expected to resist high temperatures, but also instances of hot mechanical erosion, thermal shocks, mechanical stresses, and chemical corrosion by gases, liquid oxides, and fused metals. As previously mentioned, refractory materials have additives included during the manufacturing processes to improve their response to these aggressions, as

a testament to the improvement in the production know-how and manufacturing capabilities, some modern products can have more than twelve components.

Silica-alumina

Various refractory products can be referred to as being part of the silica-alumina group.
Such as:

Fireclays are composed mainly from alumina (25 to 45%) and silica (50 to 80%). Fireclays can have their porosity varying from 8 to 24% with these properties being influenced by the firing temperature. The cold crushing strength of these products decreases considerably at higher temperatures. However, these refractories present a low thermal expansion and conductivity. The achievable temperature for these products without the loss of characteristics is around 1600 ºC, the upgrading of the alumina content increases the service temperature, as super duty fireclay (42-45% Al_2O_3) can reach temperatures of 1763 ºC, plus during service there may be the presence of small amounts of liquid-phase material without compromising the product's structural integrity. The main use for fireclay bricks is in the insolation of high-temperature atmospheres like in furnaces, regenerators, ovens, and kilns where there is no need for much structural strength.

High alumina refractories with contents of 45 to 95% of Al_2O_3 like sillimanite (61% alumina) and mullite (70-85% alumina) these products have a high refractoriness, higher slag and spalling resistance and higher load bearing capabilities in addition to a fusion point higher than 1850 ºC. High alumina refractories can be found, among other applications, in cement and lime rotary kilns, electric furnaces' roofs and glass making furnaces.
Silica refractory products are composed, as the name suggests, of high quantities of SiO_2 (>93%). Extraordinarily high resistance to thermal shocks at high temperatures (>800 ºC) and low creep, or cold flow, make the main uses of these materials the roofs of glass furnaces, and coke ovens [29], [43].

Basic refractories

This group of refractory products is distinguished by their very high resistance to corrosion by slags coupled with high refractoriness. Are basic refractories the following:

Chromite-Magnesite are refractories, where the chrome is present in a higher percentage than the magnesite, are used up to 1700 ºC and resistance to standard shocks in addition to be naturally basic. These are mainly used in applications like the inner linings of oxygen steelmaking vessels.

Magnesite basic refractories have a high refractoriness and thermal conductivity coupled with a great resistance to basic slag.

Periclase refractories (basic) with 90 wt.% MgO, 2.5 wt.%, and 3 wt.% of both SiO_2 and Fe_2O_3 (plus traces of Al_2O_3 and Cr_2O_3) and a porosity of 21-22% are commonly used in the steel-making industry thanks to their slag (liquid oxides) attack resistance [39].

Silicon refractories

Silicon carbide refractory products have a SiC content of over 85%. The main properties are high thermal conductivity and refractoriness, resistance to thermal spalling and a superior temperature load bearing capacity. These products are light weight and inert to acid slags.

SIALON are refractory materials composed of silicon nitride and alumina that after mixed are pressed (18 – 30 MPa) at high temperatures (1700 ºC) in graphite moulds in order to achieve low porosity values. The final product has good resistance to oxidation and action of molten metals, as well as resistance to borax and alkalis [43].

Silica refractories of the acid refractories family (96.3 wt.% SiO_2, and 2.2 wt.%0 plus remains under 1 wt.% of alumina, and MgO) have an apparent porosity of 25% and are well-known for their high-temperature load-bearing capabilities and therefore are used in load-bearing arched roofs of steel and glass making furnaces where temperatures can reach temperatures of 1650 ºC. At these temperatures alumina residue that may be inside the product will be in its liquid phase, as such the amount of alumina must be monitored and not exceed 1 wt.%.

Carbon refractories

These materials make use of the outstanding carbon properties. Carbon, at 3500 ºC, passes directly from its solid to its gaseous state by sublimation, it doesn't melt, and it has a good slag resistance as it doesn't get wet. It has an expansion coefficient significantly lower than that of other refractory products and superb resistance to thermal shocks, as well as a considerable range of thermal conductivity. Its chemical resistance to the majority of acids and bases is also excellent. The biggest shortcoming of the use of carbon in refractory materials is their oxidizable nature at temperatures higher than 450 ºC.

2.3.3.5 In-service refractory materials

Refractory materials maintain most of the properties of the raw materials they are made of. When choosing a refractory material to use, the decision-making starts with the raw materials, their properties, and their in-service behaviour.

Corrosion, capillary impregnation, open porosity, microstructure, and chemical composition are some of the vital considerations to take into consideration when choosing a refractory material. It is necessary to take into consideration the distribution of mineralogic phases, particle size distribution, size of crystals in the aggregates, impurities and their nature and distribution,

variation in the chemical composition of the material, presence, and location of porous and micro-fissures. All this contributes so that the more prominent properties of refractory material ca be their resistance to high temperature without melting or decomposing, as well as the ability to remain unreactive and inert.

2.3.3.6 Manufacturing process of refractory materials and products

Refractory materials can be manufactured into two basic forms, shaped and unshaped. Shaped or formed products are sold as bricks or preformed shapes, and their main utilization is walls, arches, and floors of furnaces and other high-temperature process equipment. While unshaped or unformed products consist of mortars, gunning mixes, castable (cement and concretes), ramming mixes, and plastics. This allows the products to be cured in place to form a monolithic, internal structure after application, giving the option to achieve uncommon and complex shapes.
The process of manufacturing refractory products can be divided into four main steps or processes.
Starting with **raw material processing**, this step involves crushing and grinding the raw material. In some cases, it can be required that the crushed and ground material be classified by size. Then the raw material is subjected to calcining and drying. It may finally be dry-mixed with other materials and chemicals. The processes may slightly differ for each raw material and refractory product, and some may even not be mandatory.
Next, the raw materials must be mixed and formed into the predetermined, desired shape. This process is called **forming** and frequently occurs in moist or fully wet conditions.
After the forming, the product undergoes the **firing** process, which entails heating to high temperatures in a kiln enabling the formation of the ceramic bond that provides the refractory product its properties. Lastly, the product arrives at the **final processing** stage where, due to thermal expansion during the firing process, the product must be ground and milled into the finished product with the desired size and shape. At this stage, the product may also be impregnated with tar or pitch if so desired [30], [39]. This process is presented in figure 10.

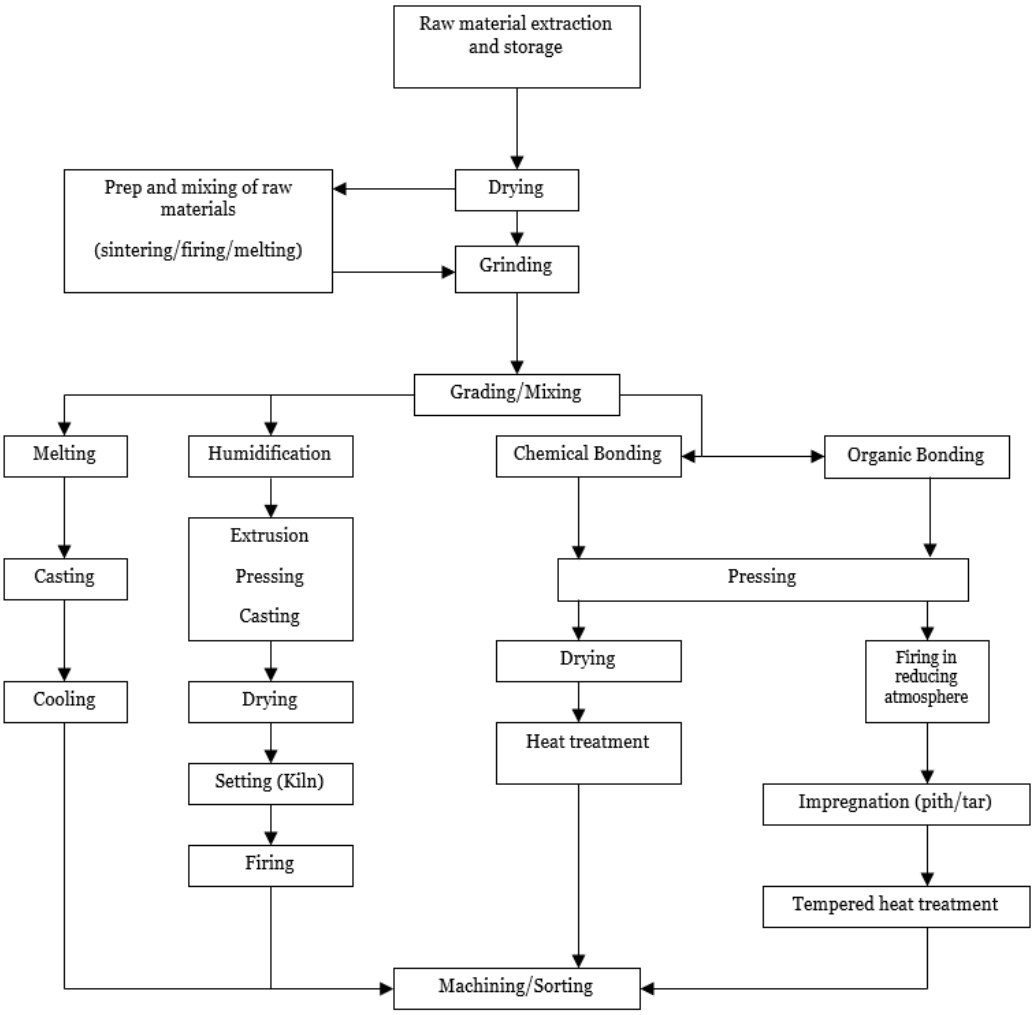

Figure 10. Refractory material manufacturing process flowchart (modified from [29]).

Chapter 3: Cases of study

3.1 HfC-SiC refractory ceramic response to hybrid rockets in highly ablative environments.

Kim et. al [31], tested the characteristics of a rocket nozzle made using HfC-SiC refractory ceramic composite, in specific the way it handled ablation. In a liquid rocket engine, the liquid propellant and oxidizer are used as a way of cooling the nozzle by directing the very cold liquid through tubes placed on the nozzle. In a hybrid rocket, however, the cooling of the nozzle grows more complicated, and as hybrid rocket engines become more popular due to their safe handling, easier use, and simpler schematics one of the areas of focus to improve performance is the study of the possible reduction and prevention of the ablative nature of the nozzles. Although the ablative materials usually used present the capacity to sustain extreme temperatures in an uncooled state during the operation of the engine, the ablation of the material that occurs, in particular in the throat area, is the main contributor to pressure drops in the combustion chamber, and poor combustion, causing drops in efficiency and performance of the engine. Therefore, the development of materials that can still withstand the high temperatures and pressures in an uncooled state and do that while suffering an insignificant amount of ablation, would mean a significant leap in the performance of the hybrid engine, facilitating stable combustion and, as such, promoting consistency in performance. Refractory ceramics like pyrolytic refrasil were studied in solid rocket engines during the nineteen sixties, this material was found to have shortcomings due to thermal shock. Furthermore, pyrolytic refrasil like silica phenolic were shown to only be able to sustain the extreme environment of rocket propulsion during limited time runs as they suffered from thermal decomposition and surface melting.

Nowadays, a new branch of ceramic materials, ultra-high temperature ceramics (UHTCs), have been developed, with extremely refractory properties, and enhanced oxidation resistance. Even though UHTCs have shown great oxidation and ablation resistance in high-temperature, and propulsion environments, there still is a small amount of testing conducted relative to the use of these ceramics as rocket nozzles of hybrid thruster engines. Materials like TaC-based, SiC-based, and fibre-reinforced ZrB_2-SiC have been studied and the results showed improved resistance to ablation, including at the nozzle throat. UHTCs do, nonetheless, have problems dealing with thermal shock due to their brittleness, as such to improve on this aspect, there have been studies regarding the addition of silicon carbide, which also adds to the materials oxidation resistance, and the strengthening of the ceramics with fibre.

In their work *Kyu-Seop Kim et. al*, studied the response of graphite and HfC-SiC composite ceramics to ablation when submitted to a test with a 250N scale hybrid rocket thruster, using 90 wt% hydrogen peroxide, and high-density polyethylene. It was concluded that the ceramic composite showed a better reaction to throat ablation than that of the ablative graphite, after-test

analysis showed that the graphite throat had enlarged by a factor of 87% relative to its initial area, while the HfC-SiC showed an increase in the area of only 19%, which lead to a more stable pressure and thrust in during the test of the ceramic composite than that the measures taken from the graphite test where, due to the increasing flow rate, the thrust increased by nearly 26% showing that ablation can have an impact in fuel consumption as well as add volatility to thrust levels. Looking at the micro-morphologies of the samples tested it was found that the graphite specimen suffered from oxidation which weakened the surface contributing to the erosion of the material. The ceramic composite had is problems also, revealing the formation of pores in the surface during oxidation which contributed to the formation of local microscale cracks meaning there is a need to develop in the thermal shock resistance and pore formation of the material. As such the use of UHTCs could help overcome ablation problems in nozzles, specifically hybrid rocket ones, with limitations relating to the size of the nozzle throat due to the brittle fracture nature of the ceramic composites.

3.2 PERSEUS/PEGASE project

3.2.2 Silicon carbide-based refractory concretes in a solar furnace

Inserted in the PERSEUS project, in which technologies are studied and developed for satellite launchers and hybrid propulsion, *Raffaele D'Elia et. al.* [44], tested, in addition to the already mentioned ablation study, the oxidation resistance, or lack thereof, of a SiC-based micro-concrete nozzle.

To this end, the material was first characterized in relation to its thermo-mechanical capabilities when subjected to temperatures of up to 1500 K, after it was submitted under a standard atmosphere and a solar flux up to 13.5 MW/m² studied the performance of the material to oxidation.

One of the factors that make silicon carbide-based ceramics a valuable material for space-related high-temperature applications is the formation of SiO_2 in passive oxidation conditions with a parabolic mass gain (first chemical equation). Still, if the partial pressure of the oxygen is at lower values than that of stability (depends on temperature) the material's substrate experiences rapid active oxidation instead, resulting in a linear mass loss and the creation of gaseous products (second chemical equation).

$$SiC(s) + \left(\frac{3}{2}\right) O_2(g) = SiO_2(s) + CO(g)$$

$$SiC(s) + O_2(g) = SiO(g) + CO(g)$$

For this particular study, there was calculated that there should be a chamber pressure of 1.7 MPa, and a contraction area ratio of 12.6 in order to emulate the conditions of the highly oxidizing environment of a hybrid propulsion rocket. The nozzle was assessed to have a throat area ratio of 4, still regarding the throat, the pressure was measured to be 0.98 MPa, and temperatures of up to 2980 K were registered during the 20-second combustion tests.

The calcium aluminate cement used is mainly comprised of alumina (70%) and has aggregates of an uncommon maximum size of 800 μm, for this reason, the authors decided to refer to this material as micro-concrete. The nozzle is then made of this micro-concrete which is composed of SiC (80 wt%), Al_2O_3(14 wt%), SiO_2 (5 wt%), and CaO (1.4 wt%). The resultant material has a density of 2580 kg/m^3.

During the test, it was observed the formation of smoke as well as the loss of mass (20.5mg/cm^2), meaning that there was active oxidation of the material. This results in a mass loss that was found to be of a linear nature in relation to combustion time.

The presence of smoke during testing also proved a challenge, impeding temperature readings by optical pyrometry.

Besides the micro-concrete, pure SiC was also tested for oxidation at 7, 11 and 13.5 MW/m^2, for which silica removal was found to happen for the latter two cases (11 MW/m^2 or higher), these pure silicon carbide results mirror those of the micro-concrete with the difference that the mass loss of the micro-concrete was far smaller than that of the pure SiC making the material developed for this study better suited for high oxidation environments, this, coupled with the fact that the micro-concrete has a lower density, increases the attractiveness of the micro-concrete for space-related applications.

The micro-concrete also has better insulating capabilities than that of pure SiC (approximately 14 W/mK versus 180 W/mK at 293 K).

Figure 11 shows the mass loss from oxidation in relation to the elapsed time of combustion for different solar fluxes for pure *alpha*-SiC and for the micro-concrete [44].

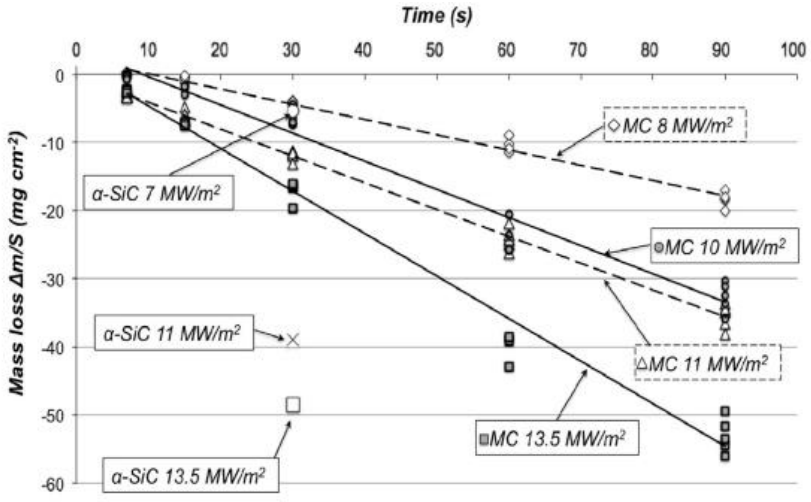

Figure 11. Micro-concrete and pure SiC mass loss for different solar fluxes graphic [44].

Figure 12 shows the microstructure of the resulting micro-cement where the SiC aggregates present a lighter grey colour while the alumina-rich, binding element, cement takes on a darker shade, furthermore we are also able to observe the porosity of the material. This material was subjected to a firing at 1473 K during a five-hour period, during which, it first went through dehydration (293 – 573 K), then recrystallization (713 – 1173 K), liquid phases formation, sintering, and densification (1073 – 1773 K).

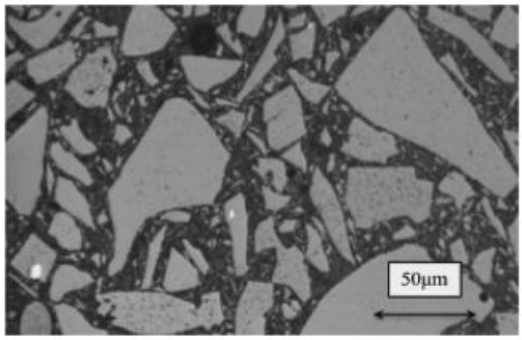

Figure 12. SiC-based micro-concrete microstructure [44], [45].

On the other hand, the next microscope cross-section image (figure 13) was taken after the sample was exposed to a solar flux of 8 MW/m^2 for 90 seconds and it shows two different areas, one where sublimation occurred as shown by the craters and the second where the effects of oxidation are prominent.

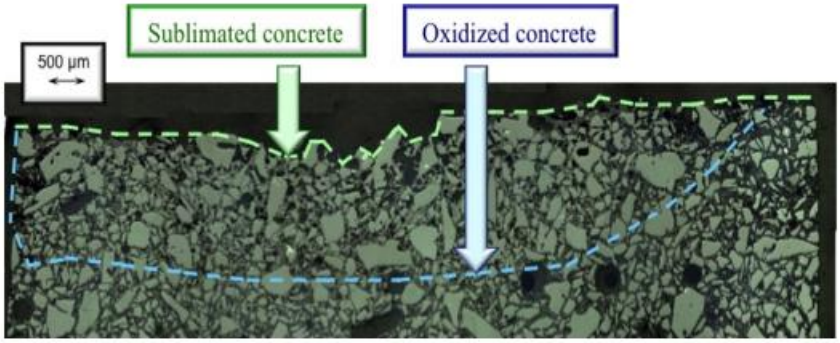

Figure 13. Micro-concrete cross-section after solar flux exposition [44].

Two more images (figure 14) from the aftermath of the tests show us the effects not only of oxidation but also (on the left) of the heating and cooling of materials with different thermal expansion coefficients such as the SiC aggregates and the binding alumina cement, resulting in visible micro-cracks, (on the right) the liquid phase appearing from, either the liquid silicon (formed at 1960 K) or the cement eutectics, between the silicon carbide aggregate and the vaporization zone, are also revealed.

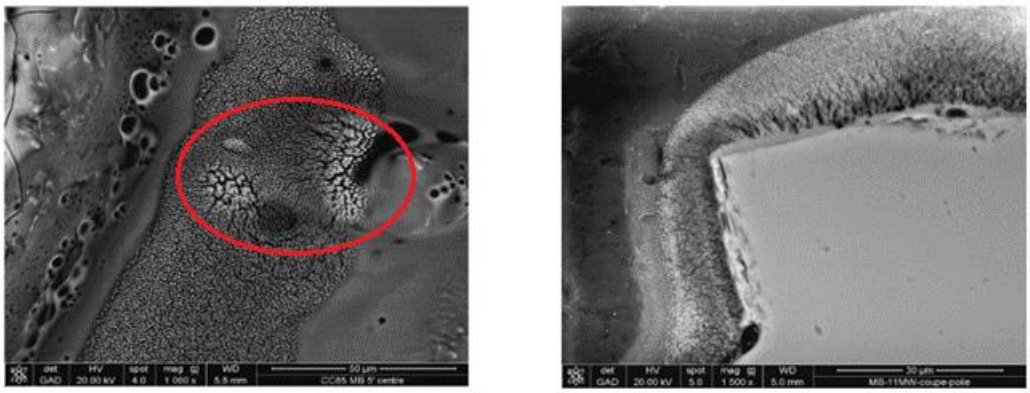

Figure 14. Micro-concrete exposed for 90 seconds on the left to 13.5 MW/m², on the right 10 MW/m² [44].

3.2.2. SiC-based refractory concrete in a hybrid rocket environment.

As in the previously mentioned work, D'Elia *et. al.* [45], noticed the lack of research on alternatives to ablative nozzles used on hybrid rocket engines, where the oxidation is greater. A nozzle made of silicon carbide-based micro concrete was developed. The nozzles used in the consequent tests were composed of 80 wt.% SiC, 14 wt.% Al_2O_3, 5 wt.% SiO_2, and 1.4 wt.% CaO, with a contraction ratio (area of the combustion chamber to throat area) of 10.5 and an expansion ratio of 4.0 (throat area to exit area). Relative to the manufacturing of the nozzles, the concrete base was mixed with water at a ratio of 8.3 wt.%, it was then poured into a resin-based mould and placed on a vibrating table for 15 to 20 minutes. Then to ensure correct hydration the piece is placed for the period of 48 hours under plastic films and at 20 °C. After the two-day process, the nozzles are removed from the mould and set during 24 hours at 110 °C as to ensure proper water evaporation. Finally, the nozzle is fired at 1200°C, a procedure that takes 5 hours, to stabilize the microstructure for testing at high temperatures, increase the material Young's modulus, and reduce liquid phase generation during the test firing.

There were three different tests realized by D'Elia et. al., where the first nozzle (HERA17) sample was submitted to a 20-second firing, the second and third (HERA18 and 20) for 10 seconds. The HERA 20 nozzle sample had steel fibres added to reinforce the concrete (1 wt.%).

The firing tests showed three phases relating to the combustion chamber pressure, the ignition phase goes from the initial firing to the stabilization of the pressure in the chamber, the combustion spans from the pressure stabilization to the sudden drop in pressure, and the shutdown that marks the very quick drop in pressure associated with the lack of oxidizer injection into the chamber. During the combustion phase the pressure can be observed to rise initially, then have a stationary zone, and then start to decrease, it's during this last phase that jet deviation was observed as well as particle ejection. Although similar observations occurred during the HERA 18 and 20 firing tests, the HERA 20 combustion phase was noted to have an almost levelled pressure throughout. This relatively stable pressure happened as a result of very little throat erosion,

unlike that of the HERA 17 and 18 nozzles. The first test had jet deviation happen after the 10-second mark caused by the asymmetrical ablation of the nozzle throat, as the flow separation wasn't observed in the HERA 20 test where ablation didn't take place. The jet deviation wasn't noticed in the HERA 18 test despite the occurrence of ablation, this may be explained by the fact that the asymmetry of the throat ablation is not as pronounced (figure 15).

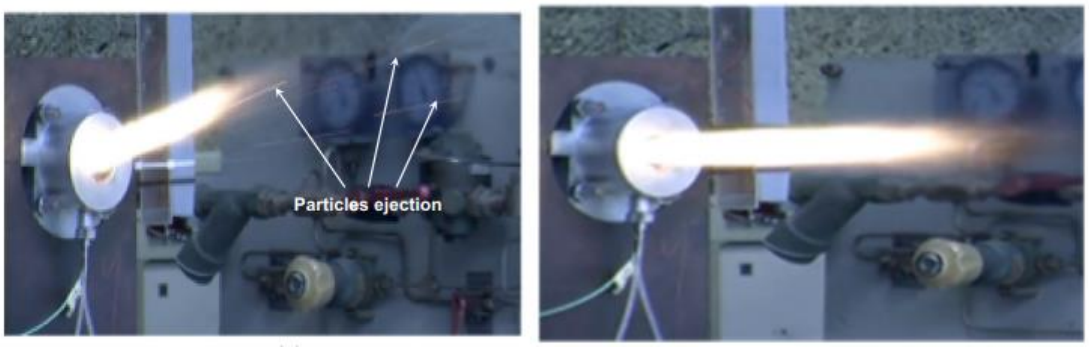

Figure 15. Effects of asymmetrical ablation on rocket nozzle [45].

The asymmetric nature of the throat area ablation (figure 16) may be exaggerated by gravity, as the tests were conducted in a horizontal position, this wasn't, however, confirmed with experimental procedure.

There was also the formation of cracks in the HERA 17 and 18 nozzles but not in the fibre-reinforced one. The previously mention manufacturing process allows through the vibration of the samples to randomly set the fibres throughout the nozzle which helps prevent the ceramics brittle behaviour.

The addition of short metallic fibres to the SiC-based concrete nozzle was shown to enhance thermos-mechanical resistance under the test environment presenting this material as a possibly viable alternative to the normally used graphite and refractory metals, especially if the material is surface treated to improve oxidation resistance.

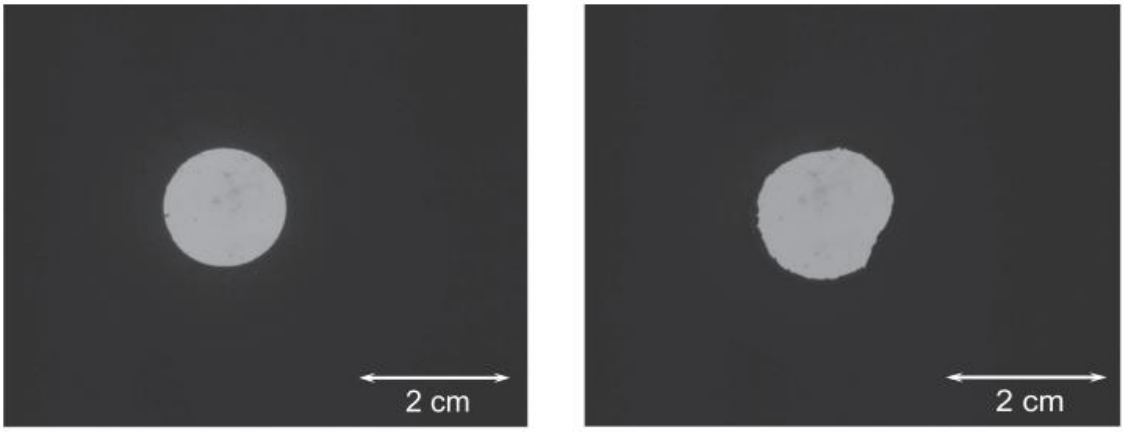

Figure 16. Asymmetrical ablation of a nozzle throat [45].

3.3 Novel ceramic composites for rocket nozzles in harsh environments

With the intention of characterizing ultra-high ceramic matrix composites (UHTCMC) materials for near-zero erosion rocket nozzles, *Stefano Mungiguerra et. al.* [38] devised two test set-ups in a representative environment, characterized by relevant heat flux and temperature, for preliminary screening of materials, where a hybrid rocket engine (200 N) using oxygen in its gaseous form and high-density polyethylene as propellants. One test consisted of placing small button-like samples (17 mm diameter) of the materials such as to be directly hit by the exhaust jet plume of the rocket nozzle at a distance of 15 cm, in the second, the material was made into chamber inserts, shaped as an annular piece, and placed inside the rocket combustion chamber. The setup is shown in figure 17 taken from the paper.

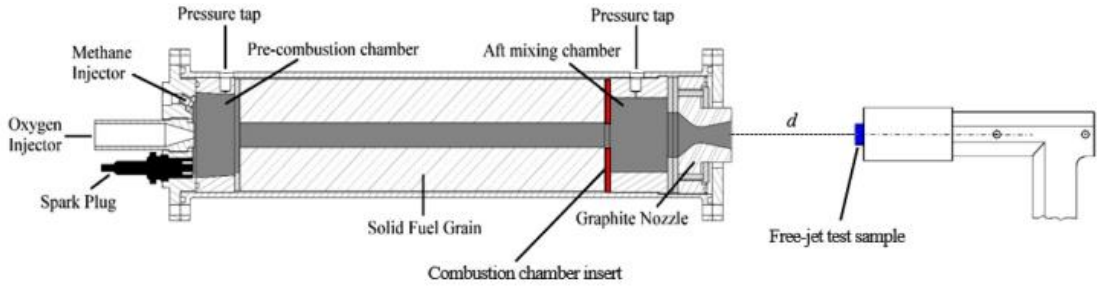

Figure 17. UHTCMC characterization two test setups [46].

The first test configuration was selected as the conditions the sample experienced were found to be realistic when compared to those found in a nozzle exit section in terms of the heat flux (15 MW/m^2), temperature (above 2500 k), and gas compositions (oxidizing and chemically reacting atmosphere) experienced by the material, while simplifying the manufacturing of the samples. The second test was designed with manufacturing simplicity in mind as well while being able to emulate the typical conditions the material would experience in the combustion chamber of a hybrid rocket engine, such as higher pressure in the region of 10 bar, and a heat flux of about 5 MW/m^2. It is worth noting that the test did fail to replicate gas velocities as high as those experienced in a real combustion chamber application of the material.

The UHTCMC material was prepared using ZrB_2 as the matrix with SiC added (10 vol%) as well as pitch-derived carbon fibres. Three different samples were prepared for the first test, two using slurry infiltration of carbon fibre fabrics, with a 0/90° stacking configuration but each using a different method of sintering, either Spark Plasma Sintering or Hot Pressing, the third sample was manufactured using chopped fibres milled to the ceramic powder. It's noteworthy that the two long fibre samples, due to the different sintering processes, ended up having different porosity, the first having less than 1 vol% while the second had 11 vol%. As for the case of the

second test, there were two inserts made, one using long carbon fibres and the other using short fibres.

The results of the first test (figure 18) show that for identical test conditions, the long fibres high porosity sample maximum temperature was over 400 K lower than those reached by the other two samples whose temperature started rising increasingly fast after 4-5 seconds reaching 2800-2900 K, furthermore, after this sudden rise in temperature, there was the ejection of solid fragments from the surface of these two samples. The high porosity long fibre sample, on the other hand, did not experience this instability. Still, even the two samples that did experience instability felt an erosion rate lower than half of that experienced by the graphite control sample. Through the analysis of the post-test pictures of the samples it seems that the samples all suffered from oxidation due to the exposure to the supersonic exhaust but it is clear that the high porosity piece managed to maintain its structural integrity through the thermos-mechanical loads it suffered while the other two didn't.

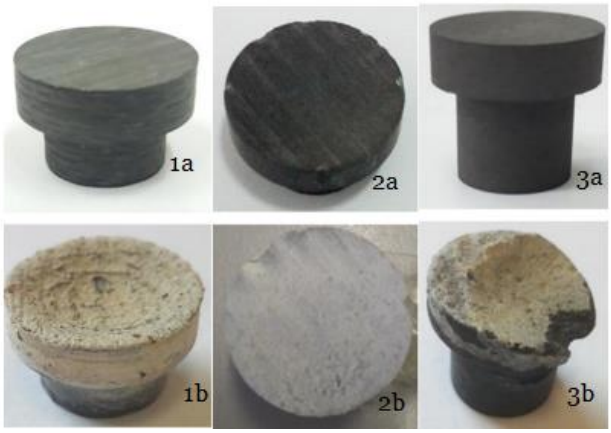

Figure 18. Before (a) and after (b) the test of samples with long fibres low porosity (1), long fibres high porosity (2), and short fibres (3) [46].

Concerning the chamber insert test (figure 19 and 20), there was a control run to have a reference to compare the results of the two UHTCMC sample tests, this control was run with a classical C/SiC disk. After this control the C/SiC disk showed signs of suffering significantly from erosion, as demonstrated by the throat that was originally 15 mm in diameter and after the test was measured at 20.6 mm. Additionally, the pictures taken after the test, in conjunction with the knowledge that these types of CMC tend to have low interlaminar strengths, give an indication that even though no cracks were detected, there is reason to be concerned about the structural resistance when using such materials.

In contrast, the long fibre chamber insert after the test did show oxidation on the exposed surface to the flow, but the throat did show considerable resistance to material erosion and to possible structural failures, having nothing but slight deposit and surface roughening.

The sample with short carbon fibres did not hand the test nearly as well as the long fibres one, whereas the throat diameter was similarly maintained, the disk suffered critical structural cracks

from which combustion gasses leaked creating terminal damages to the engine itself. The performance of the different test samples can be largely attributed to the different thermal shock resistance of the material resulting from the difference in sintering conditions, the long fibre disk having a porosity of around 15 vol% after sintering was able to suffer no structural damage, while the disk with short fibres behaved as a brittle ceramic ultimately ending up cracking.

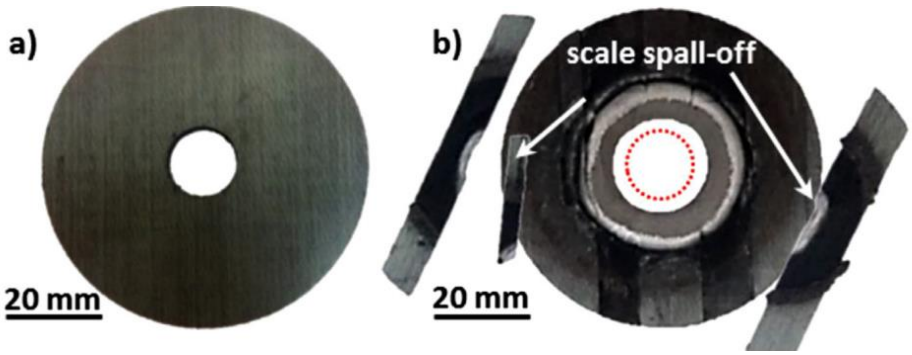

Figure 19. a) Disk Insert before Testing b) C/SiC disk after testing. In red the original diameter of the throat.

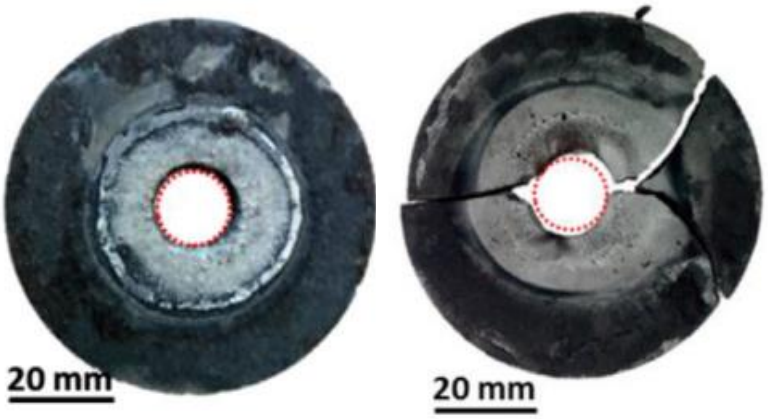

Figure 20. Aftermath of the test on the long fibre (left) and short fibre (right) UHTCMC disks [46].

In general, all the tests confirmed, when compared to the control state-of-the-art materials, that the ZrB_2-based UHTCMCs reinforced with carbon fibres, appeared capable of withstanding harsh environments, such as hybrid rocket applications, especially when manufactured with meticulously controlled processes in other to obtain the desired optimal mechanical properties.

Chapter 4: Experimental procedure

This experimental procedure encompasses everything starting with the choice in nozzle geometry, the design and fabrication of the mould(s) and nozzle samples, and the testing of these.

4.1 Nozzle Design

4.1.1 Geometry selection

As previously stated, rocket nozzles can have varied geometries, ranging from a simpler design like the conical nozzle to more complex, albeit better performing, ones like an aerospike or a dual bell nozzle.

As for this work, however, the main priority is to study the characteristics and capabilities, of the material from which the nozzles are composed, as well as their influence to maintain performance when subjected to the extreme environment that is rocket propulsion. The conical nozzle geometry was therefore the first and most obvious choice, mainly because of its fabrication simplicity.

The conical geometry designed was not optimized as that was not the intended objective, furthermore the nozzle samples will be produced to be tested in a stationary rocket engine meaning that there won't either a variation in atmospheric pressure, or the need for the system to be efficient in delivering thrust.

The nozzle was then projected with a 20 mm diameter opening to connect to the rocket engine, the diameter of the throat having 10 mm, the α angle of around 14° (near the 15° mentioned in the conical nozzle subchapter), the total length is of about 70 mm (50 mm from throat to exit) as seen in figure 21.

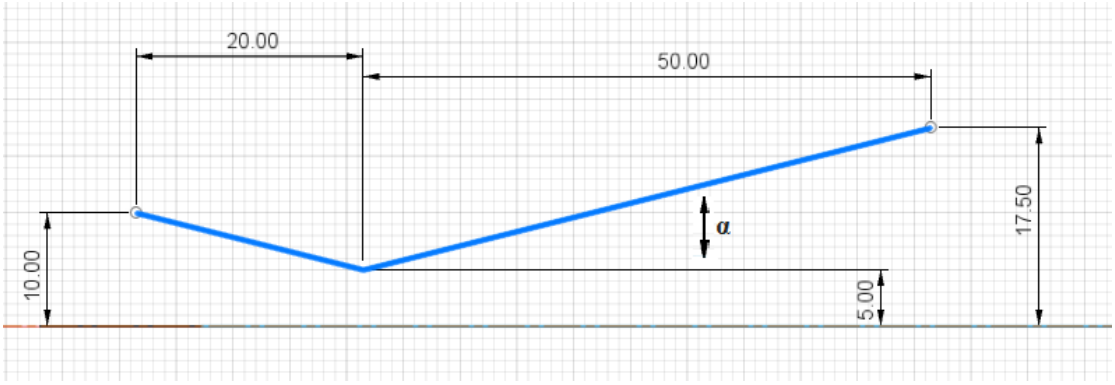

Figure 21. Nozzle interior profile and measurements

4.1.2 Nozzle design and mould printing

4.1.2.1 Nozzle initial design concepts

The nozzle and respective mould were designed utilizing the CAD software program SOLIDWORKS initially but then FUSION 360 instead. In the first stages of projecting the nozzle, different options and geometries were designed in order to better visualize and then decide.
From the start it was decided that the nozzle should have a thicker wall in the area of connection to the rocket engine as this would allow not only for a better response to the mechanical stresses that the nozzle might experience as well as make it easier to connect the nozzle to the test rig.
The first stage of the nozzle design was of a simpler nature, with an interior geometry that had a smooth curve from the converging zone to the throat and continuing to the exit, as shown in figure 22.

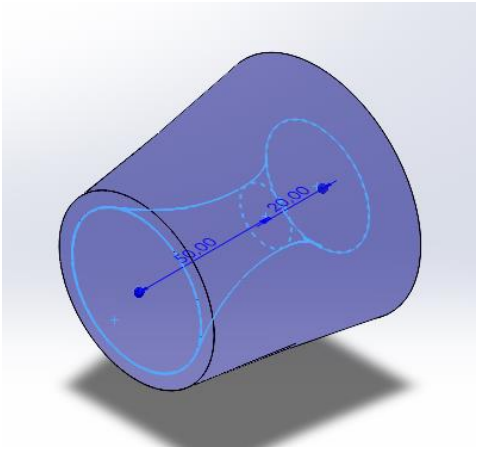

Figure 22. Initial, simpler, nozzle design in SolidWorks.

This design was then worked on until the design of figure 23 was reached, where the throat was more pronounced and with an angle from throat to exit closer to the 15º.

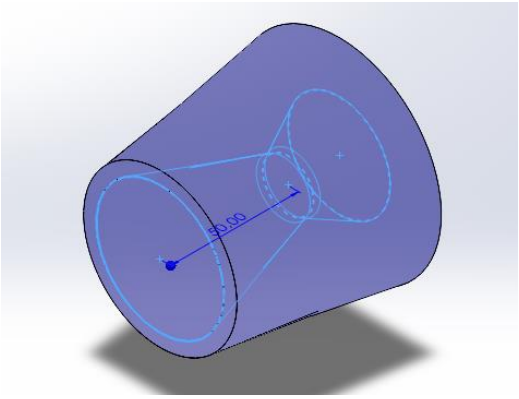

Figure 23. Better defined throat design in SolidWorks.

After that a different design, was made, where the geometry resembles a bell configuration (figure 24), this option was then discarded as the simplicity of figure 23 was found to better suit the objectives of the study, as these nozzles would only be used in static firings, meaning that the optimization of the thrust output wasn't a priority. Additionally, looking at the table 1 distinguishing factors between the bell and conical geometry, the main differences are the length of the nozzle, an optimized conical nozzle tends to be longer than a similar bell nozzle, and the direction of the plume flow, the bell nozzle due to its shallower exit angle leads to a flow that is closer to the nozzle's axial direction. Since the critical point of the nozzle material degradation is generally the throat, as shown in the study cases, the conical nozzle geometry was found to be suited to this study.

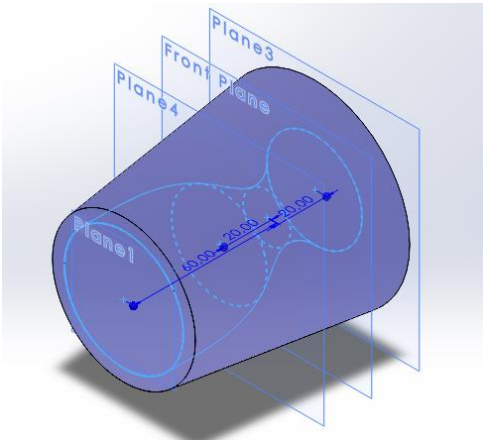

Figure 24. Bell geometry nozzle option in SolidWorks.

At the early development the option to have holes as a means of connecting the nozzle to the rocket engine test bed was considered, this is shown in figure 25. Later the decision to use, instead, a step was found to be favoured as it presented a safer option of stress distribution.

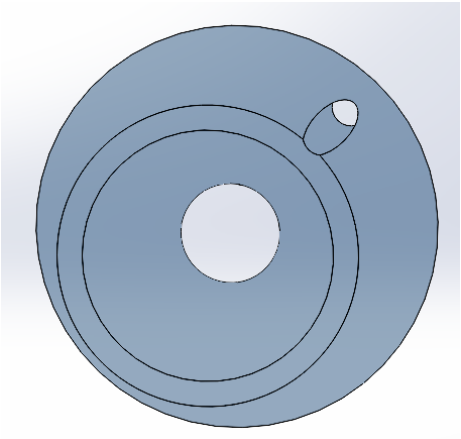

Figure 25. Early-stage hole connecting nozzle in SolidWorks.

4.1.2.2 Mould design

The mould creation process started with the figure 23 concept in mind, as such the mould was deigned to be a negative image of its geometry. Starting with the critical part, the interior aspect of the nozzle (figure 26), a piece was designed with the dimensions shown in the point 4.1.1.

Figure 26. Interior pieces (convergent section in yellow and divergent in grey) of the nozzle mould.

This part was divided into two pieces, the converging and diverging section, in order to make it possible to retrieve it without inflicting damage, making it reusable. It can also be noticed the presence of a 2 mm deep extrusion in the base of the piece, the finality of such a design component is to not only allow the assembly of the final mould in a single base but also to guarantee concentricity within the mentioned base with the outer part of the mould.
The base was then made to accommodate the male and female mould components in a way to not only secure them in place but, as already acknowledged, to guarantee concentricity between the different mould parts. This resulted in a circular base with 2 mm deep intrusions where the female and male parts fit as seen on the figure 27.

Figure 27. Mould base with mounting intrusions.

The outer walls were made with a “step” as a solution to connect the nozzle to the rocket engine (figure 28), this can be seen in the image of the mould, additionally, this part of the mould was

also cut in half as to assure an easier extraction of the nozzle from the mould, ensuring the ability to reutilize the mould for more than one samples.

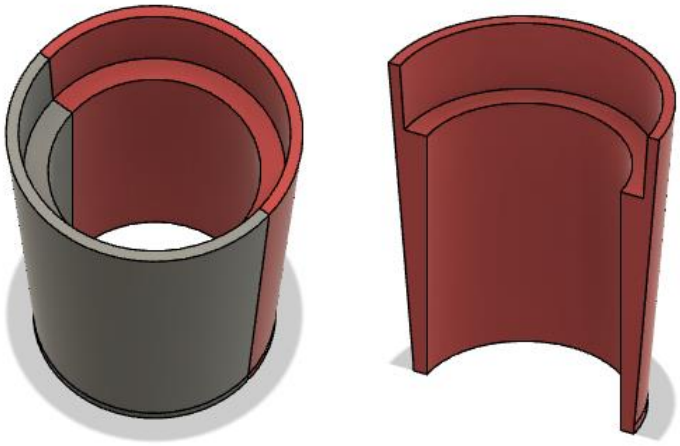

Figure 28. Outer components of the nozzle mould divided in two pieces for easier demoulding.

The top or cap of the mould was made to be another way of securing the female section of the mould. In figure 29 can be seen four cuts in the cap with the finality of providing where to pour the cement into as well as to save 3D printing material.

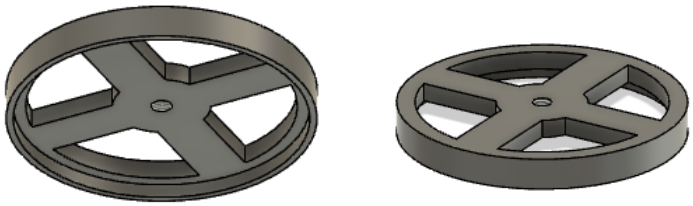

Figure 29. Mould cap with four holes to facilitate the mould filling process.

Before printing the mould, a hole was added, in the middle, that transverses the mould from when into the other as a way of not only joining the pieces and avoiding any expansion or deformation of the mould, as well as a fail-safe manner of certifying concentricity. A tolerance of 0.1 mm was added to each side in points where the pieces joined to enable the pieces to fit together, as seen in figure 30.

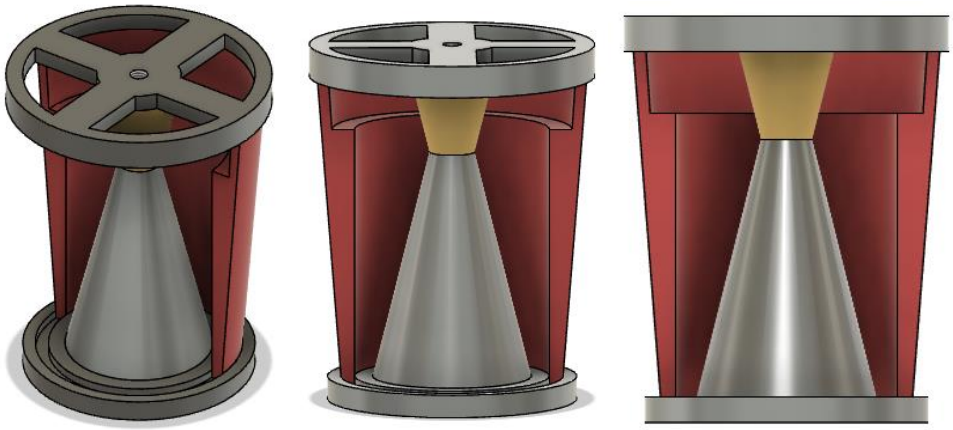

Figure 30. Complete mould without one of the outer pieces to enable viewing the interior.

The pieces were then printed in a 3D printer using a *Stratasys uPrint SE* printer and ABSplus (ABS- P430XL Model in Ivory from *Stratasys*) filament as an option to make the mould harder. The male pieces required extra attention as the nozzle interior, where the exhaust flow of the rocket engine will pass through, is an area of critical importance, thus these parts of the mould (figure 31) needed to be sanded under water to achieve a smoother surface without heating the material to the point of melting.

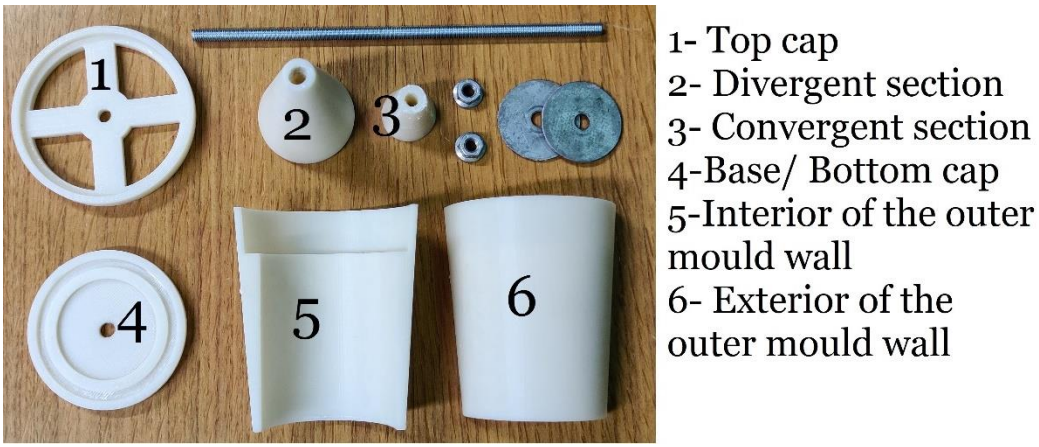

Figure 31. Disassembled 3D printed nozzle mould.

A threaded rod with 5 mm of diameter, two M5 nuts and washers were used to complete the assembly of the mould as shown in figure 32.

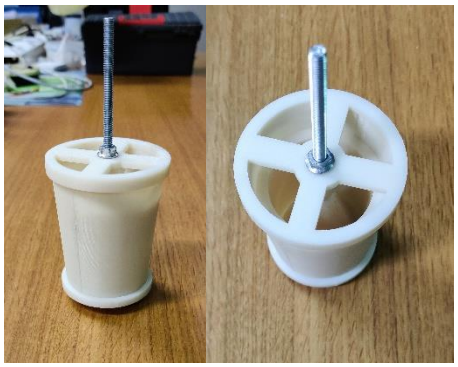

Figure 32. Assembled 3D printed mould.

While designing the nozzle, a version mould was also 3D printing with a smaller exit diameter (figure 33 and 34) of 25 mm and consequently a smaller α angle (around 8º). That nozzle was utilized as a testing piece to initially understand and later enhance the mixture fabrication and the filling and demoulding processes. The intuit was also to try and understand if a difference in the divergence angle and overall size of the nozzle exit could influence the throat response to the extreme rocket propulsion environment.

Figure 33. Smaller α angle 3D printed nozzle mould, disassembled.

Figure 34. Smaller α angle 3D nozzle mould assembled.

4.2 Materials

4.2.1 Materials selection

From an early stage it was planned that one of the tested nozzles was to be composed of almost entirely alumina. Alumina is an already proved and tested refractory material and as such is an exceptional candidate for a control nozzle sample. Nevertheless, the utilization of a refractory ceramic composed of alumina in the specific context of a rocket nozzle is of interest, especially considering the application of commercial grade alumina.
The materials used in the creation of the alumina nozzle are presented in the following table 10.

Material	**Composition [%]**					
Alumina	Al_2O_3	Na_2O	SiO_2	Fe Magnetic		
Tabular alumina T60/64 0-0.2 mm/ 0.2-0.6 mm/ -230 mesh (0.063 mm).	99.5	<0.4	<0.09	<0.02		
	Al_2O_3	Na_2O	SiO_2	Fe_2O_3	MgO	CaO
Reactive alumina CT 3000 LS SG	99.8	0.03	0.015	0.015	0.040	0.015

Calcium Aluminate Cement	CaO	Al_2O_3	Na_2O	SiO_2	Fe_2O_3	MgO
CA-25	17-19	>78	<0.6	<0.3	<0.2	0.4

Table 10.Composition of the different types of alumina and cement used in the alumina nozzle mixture [48]–[50].

Tabular alumina (T60/64)

The tabular alumina (AT) used is a pure sintered α-alumina fully densified by rapid-sintering at temperature above 1800 ºC. The AT has outstanding thermal shock resistance, and thermal volume stability. In addition, its microstructure, with low open porosity and large crystals, imparts in the AT an extremely high refractoriness, mechanical strength and abrasion resistance. Chemical purity, and good resistance against acid and alkali corrosion are all characteristics that make tabular alumina very attractive to the application in this study (table 11).

The AT has a density of 3.50 g/cm^3 and a maximum water absorption percentage of 1.5% [47].

Class	**Size distribution [mm]**	**Typical (Min/Max) [%]**
AT 0-0.2 mm	+0.212	3 (0-5)
	+0.125	12
	+0.063	38
	-0.045	41 (25-55)
AT 0.2-0.6 mm	+0.71	1 (0-2)
	+0.5	11
	+0.25	81
	-0.212	3 (0-7)

Table 11. Size distribution of the two tabular alumina classes used [49].

Reactive alumina (CT 3000 LS SG)

The reactive alumina CT3000, for high sintered density and low impurities requirements, is a special purpose low soda high reactive alumina that combines low impurities with high fired density (table 12) [48].

CT 3000 LS SG Properties	Average Values
Specific surface area [m^2/g]	7.80
Particle size (D50) [µm]	0.5
Particle size (D90) [µm]	2.0
Density * [g/cm^3]	2.24
Shrinkage (1540 ºC/1600 ºC) [%]	16.8/17.3

Table 12. Properties of the reactive alumina CT 3000 [50].

*Density presented in the manufacturer datasheet differentiates from the previously tested in laboratory which is the value used and presented in this study.

Calcium aluminate cement (CA 25)

Calcium aluminate cement is a binding agent in our mixture. The CA 25 is a cement used in the refractory industry for castables that require fast setting times with early strength development. The typical CA 25 cement properties are laid out in table 13:

CA 25		Average value	Minimum	Maximum
Water addition [%]			10	
Setting time [min]	Initial Setting		50	
	Final Setting	70		90
Cold modulus of rupture [MPa]	24h Cured at 20 ºC	6	4	
	24h Dried at 105 ºC	8	5	
	5h Fired at 1000 ºC	6	5	
Cold crushing strength [MPa]	24h Cured at 20 ºC	35	21	
	24h Dried at 105 ºC	40	26	
	5h Fired at 1000 ºC	30	22	

Table 13.CA 25 cement properties [48]

Having decided to use alumina as the well-known, well-performing refractory material, the opportunity presented itself to employ waste material from the Panasqueira mines and fly ash from the Pego thermoelectrical plant for the other nozzle as a possible reutilization of throw-away material. Looking at the constituent components (table 14) of these materials and realising that Al_2O_3 and SiO_2 comprise the majority of the composition of both materials, there was interest in testing these materials as a sustainably friendly alternative to refractory materials in the context of rocket engine environments, as an alternative usage to otherwise discarded by products.

Material	Na_2O	MgO	Al_2O_3	SiO_2	SO_3	K_2O	TiO_2	Fe_2O_3	CaO
Panasqueira mine waste (PAN)	0.48	3.89	19.45	57.07	1.39	5.08	0.87	11.77	
Pego plant fly ash (ASH)	1.01	1.75	24.49	59.19	0.82	2.87	1.33	7.14	1.40

Table 14. PAN and ASH materials chemical compositions.

There are various noteworthy elements present in both materials like the, wanted, aforementioned, alumina and silica (mullite), and the small amounts of titania, and the unwished-for sulphur trioxide and potassium oxide, the presence of which must be carefully maintained to small quantities because of the nature of these components and the tests the materials will be subjected to.

The alumina nozzle and material will be represented by ALU while the PAN waste and ASH material mixture and nozzle will be represented by PA.

4.2.2 Material characterization

4.2.2.1 Materials density

Although the cement, commercial and reactive alumina have a manufacturer provided datasheet with properties, the Panasqueira mine waste and the Pego plant fly-ash materials needed to be characterized regarding their density and particle size distribution, so tests were run.
In order to quantify the density of the materials, a *Chatelier* volumeter was utilized (figure 35).

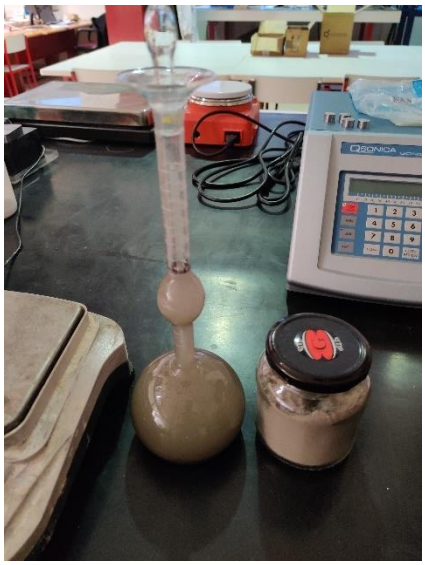

Figure 35. Fly-ash density test using a *Chatelier* volumeter.

First distilled water was poured into the volumeter until it reached the zero mark, the water filled volumeter was then weighted. Then the fly-ash was added into the volumeter, and the device rotated at an angle in order to avoid the formation of air bubbles and retrieve the few that appeared. Finally, the volume and mass were read from the fly-ash and water filed volumeter (figure 36). Subtracting the weight of the water-volumeter system from the ASH filled volumeter we obtain the mass of the fly-ash present inside the volumeter which by dividing by the volume read gives us the density of the fly-ash material in grams per centimetre cubed.

Figure 36. Fly-ash density calculation process utilizing a weighing scale and *Chatelier* volumeter. From left to right: Water, and water and fly-ash filled volumeter weighing, and fly-ash volume reading.

The PAN material was subjected to the same test, the obtained results (table 15) were as follows:

Material	Mass [g]	Volume [cm³]	Density [g/cm³]
PAN	55.2	19	2.89
ASH	41.21	18	2.29

Table 15. PAN and ASH average density test measurements and results.

4.2.2.2 Material size distribution

The particle size distribution was found using a laser granulometric analysis equipment (Beckman Coulter, LS200). The results for all materials utilized in this experimental procedure are then presented in the following cumulative particle size distributions graphics (figure 37).

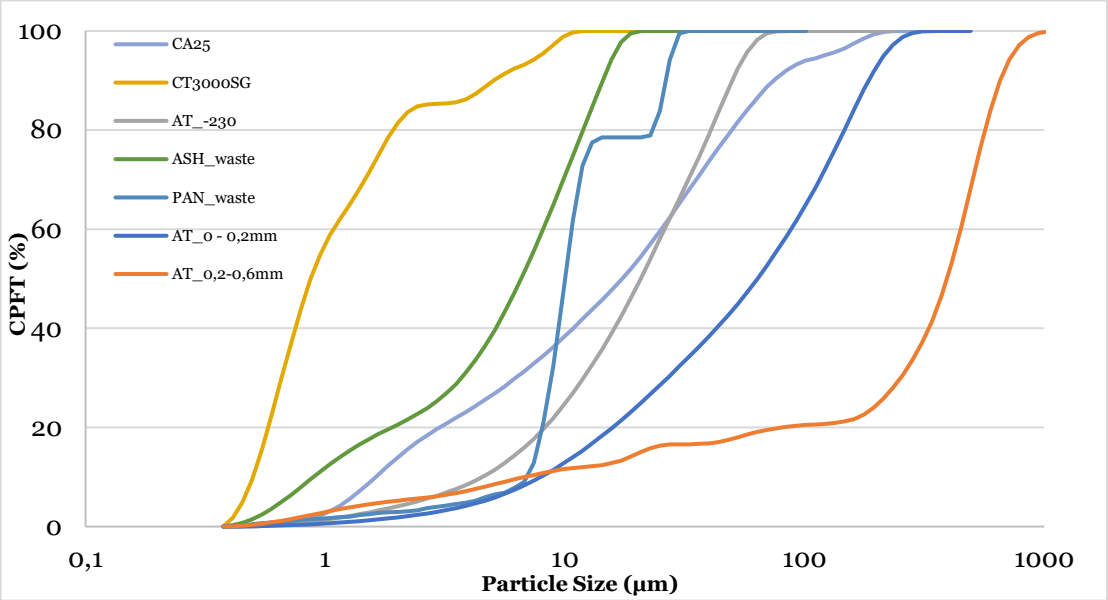

Figure 37. Particle size distribution for the materials used.

The graphic displays the percentage of particles that are finer than (CPFT) a determined particle size (in microns). Studying the curve of the tabular alumina AT 0,2-0,6 mm, for example, it can be determined that 80% of the particles present in this material are between the size of 100 and 1000 µm, while in the case of the finer material, the reactive alumina CT 3000 SG, it can be deduced that 80% of the particles are finer than ~2 µm. We can also read the graphic from left to right to obtain the order of the materials from finer to larger relative particle sizes.

This information will be vital to be able to understand and be able to modulate the mixtures particle packing and therefore the fabrication of the cements that are to be poured into the moulds.

4.3 Mixtures

4.3.1 Packing models

The distribution in particle size influences the properties, for instance, the viscosity, the permeability and the time required for the cement to fully dry. On account of the works of the likes of Furnas, Andreasen, Westman, and others, there were developed models of packing that make possible the manipulation of the processing of ceramic materials as to attain the desired properties. The particle size distribution also impacts the final properties of the ceramic material. The density (and porosity), and particularly the mechanical resistance.
To understand the packing of particles the utilization of a graphic of differential or cumulative volume in relation to the particle size. In these graphs the cumulative curve, also commonly known as CPFT (cumulative percentage finer than), expresses to each particle size of the distribution, the ratio of particles smaller or bigger than that size.

4.3.1.1 Furnas packing model

Furnas' model is based on the simplest form of particle packing, in which at the start there is only a class of single size spheres or particles, and to each new single size classes are added, each with sizes that adjust to the initial interstices. This is repeated until the porosity is infinitely small. Furnas then states that the efficiency of the packing of particles in a three-class distribution (fine, medium and coarse) depends on the efficiency of the packing of the particles in each class.
In extrapolating this from a simple three class distribution to an infinity of discrete size classes, the efficiency of the packing of a continuous distribution is then defined by the following equation 4:

Furnas' model:

$$CPFT = \frac{R^{\log D_1} - R^{\log D_S}}{R^{\log D_L} - R^{\log D_S}} \times 100 \quad (4)$$

With the cumulative percentage finer than (CPFT) being in relation to "D". D_1, D_L and D_S meaning the size of the actual particle, the biggest particle size, and the smallest particle size respectively. And R represents the volume ratio between the intervals of adjacent particle sizes.
This packing model does however stray away from what is considered realistic by natural occurrence, as particles in a more diverse variety of sizes enable the formation of high-density mixture. Moreover, a system with a continuous distribution of sizes, in opposition to a discrete one as in Furnas' model, display better properties, such as, enhanced mechanical resistance.

4.3.1.2 Andreasen packing model

Andreasen's method is based on building similar conditions to those of the perfect particle packing and is, therefore, presented in an equation (5) that designates a behaviour such as that displayed in nature.

Andreasen's model:

$$CPFT = \left(\frac{D_1}{D_L}\right)^q \times 100 \qquad (5)$$

Where CPFT is usually presented as a logarithmic function of "log (D)", which shows as a linear graphic of inclination q (modulus of distribution). By "D" is meant the particle size in milometers, as by "D1" and "D_L" the actual particle size and the larger particle size respectively. The correlation between the distribution modulus and particle size is that of proportionality, when the ratio of large particles is higher so is the "q" [49].
Additionally, the modulus of distribution must be of values between 0.33 and 0.5 in order to find the packing close to ideal, and guarantee a minimum fluidity of the mixture.

4.3.1.3 Alfred's (Andreasen's modified) packing model

Alfred's model, also known as Andreasen's modified packing model appeared in the late 20th century with the introduction of a minimum particle size distribution to the original Andreasen's model by Funk and Dinger. This modified the equation (5) to include D_s (minimum particle size) as shown in equation (6).

Modified Andreasen's or Alfred's model:

$$CPFT = \frac{D_1^q - D_S^q}{D_L^q - D_s^q} \times 100 \quad (6)$$

Even thought, a q in the other of 0.33-0.5 might represent a close to ideal packing of particles, in applying it, porosity along with other characteristics like viscosity and fluidity of the cement or paste may be required. To prevent a very dense packing of the ceramic material after the processing of the paste, a modulus of distribution of 0.37 may be used. However, q values of 0.21 to 0.22 are suggested to be used for an improvement in fluidity as it prevents the development of large-particle formations that tend to stagnate the flow of particles. The packing models are presented in figure 38 in their graphic representation.

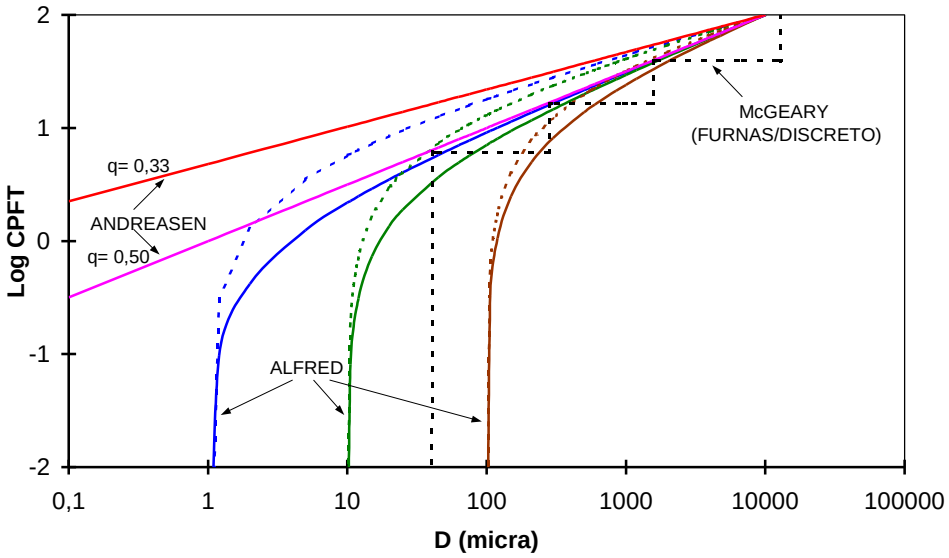

Figure 38. Graphic examples of the different packing models (Furnas, Andreasen, and Alfred). Modified form [50].

4.3.2 Mixture modulation

As the constituent materials of the nozzle's ceramic mixture are of different coarseness, there is the need to optimize the quantities of each material, and therefore size, as to ensure the desired flowing conditions and homogeneity of the mixture. The EMMA (Elkem Materials Mix Analyser) [51]software was used to this end, after the properties of each material, the size distribution of its particles, selected from a library of previous works, and its density were introduced into the software, the Andreasen's model was selected with a distribution modulus of 0.22, a value selected in order to make a flowing mixture and not to dense, from the previously mentioned interval of 0.21-0.22 the higher value was chosen to avoid brittleness and most importantly to diminish the thermal contraction during the ceramics drying process as the dimensions of the rocket nozzle interior are of extreme importance, mainly in the connection to the engine test rig.
After that the optimization process is made by slightly alteration the values of quantity of each component until the particle size distribution curve resembles the Andreasen's model line (figure 39).

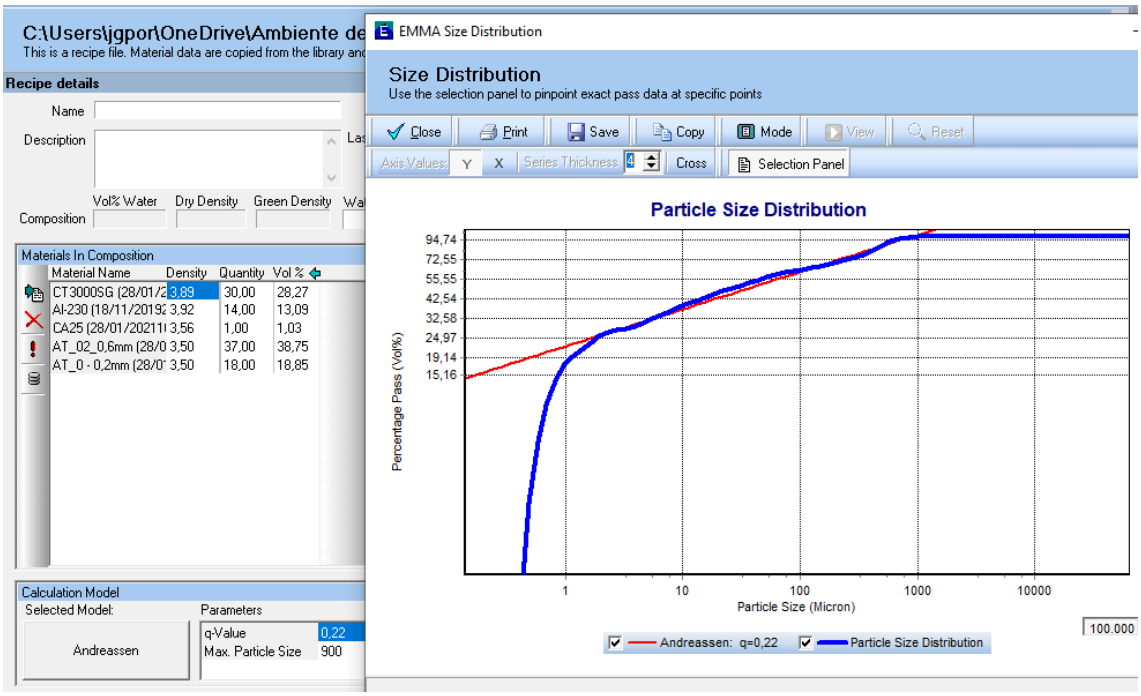

Figure 39. Optimization of the particle size distribution for the alumina mixture in the EMMA software. Left: List of materials and their density, quantity, volume percentage, packing model selection, q value and maximum particle size. Right: Theoretical Andreasen model curve (red) and real mixture particle size distribution curve (blue).

The fractions of each material in the alumina nozzle mixture obtained by optimization in the EMMA software are thus presented in table 16:

Material	Mass fraction (%)	Class	Quantity (g per 100g mixture)	Volume fraction (%)
Reactive Alumina	30	CT 3000 LS SG	30	28.27
Tabular Alumina	69	Al -230 Mesh	14	13.09
		AT 0-0.2 mm	18	18.85
		AT 0.2-0.6 mm	37	38.75
Calcium Aluminate Cement	1	CA 25	1	1.03

Table 16. Alumina mixture composition optimized in the EMMA software.

Given the composition of the different materials presented in table 7 the final mixture of table 16 will be around 99.4% Al_2O_3.

As for the ASH and PAN waste nozzle (PA nozzle), the option was made to try and substitute part of the reactive alumina with the ASH material, as the CT 3000 SG alumina is prone to contracting more during the drying and firing process (sintering) which can damage the piece and is therefore an unwanted characteristic of the material, besides, the reactive alumina is a more expensive

product than the AT and the ashes are the material that has a closer particle size distribution to that of the CT 3000 SG. The PAN waste has a difficult to work with particle size distribution, hence this material was used in a lesser quantity of 4 wt.% taken from the -230-mesh alumina, as a way to try and maintain the mixture's particle size distribution as close as possible to the optimized packing model (figure 40).

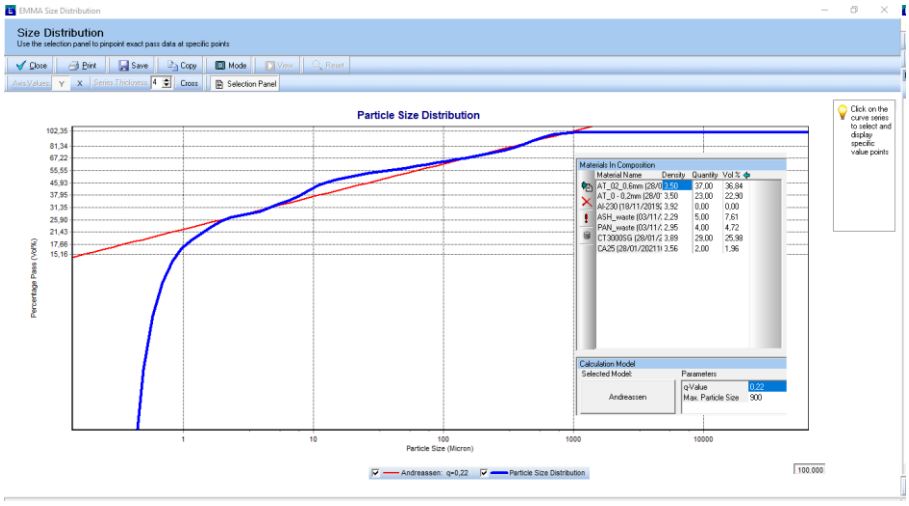

Figure 40. Optimization of the particle size distribution for the ASH and PAN mixture in the EMMA software. List of materials and their density, weight percentage, volume percentage, packing model selection, q value and maximum particle size, and theoretical optimized q =0.22 Andreasen model curve (red) and real mixture particle size distribution curve (blue).

The ashes and mines waste mixture, shown in the table 17, are clearly further from optimization than the alumina mixture as the materials, mainly the PAN waste, have particle size distribution not as consistent or predictable as the commercial alumina. This may be due to a big step in mesh size in the material sorting process.

Material	Mass fraction (%)	Class	Quantity (g per 100g mixture)	Volume fraction (%)
Reactive Alumina	29	CT 3000 LS SG	29	25.98
Tabular Alumina	60	Al -230 Mesh	-	-
		AT 0-0.2 mm	23	22.90
		AT 0.2-0.6 mm	37	36.84
ASH waste	5	-	5	7.61
PAN waste	4	-	4	4.72
Calcium Aluminate Cement	2	CA 25	2	1.96

Table 17. PA mixture composition as optimized in the EMMA software.

4.4 Nozzle and Mixture fabrication

4.4.1 Nozzle manufacturing process

4.4.1.1 Alumina nozzles

The process of production of the mixture started with the previous point of the packing models, from that point, the materials were weighted (on a *Nahita Blue* electronic balance Series 5162 with a readability of 0.1 g and a maximum load of 2 kg) in accordance with the quantities presented in the table 16 but for a 1-kilogram mixture (figure 41).

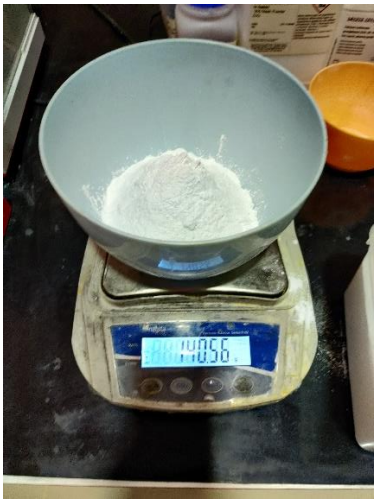

Figure 41. Addition of 140 grams of Al -230 into the mixture.

At the end, a small amount of citric acid was added (figure 42) into the dry mixture to avoid the formation of particle clusters. This citric acid evaporates, and it doesn't affect the final mixture.

Figure 42. Addition of citric acid to avoid cluster formation.

Having added all the materials, the dry mixture was then put in a stand mixer (*Tecnotest* model B205/X5). With the mixer running, distilled water was slowly poured into the mixture, at first 50 grams (5 wt.% of the dry mixture) to which was later added, after verifying that the mixture was still not a homogenized paste, more 15 grams totalling a water to dry mixture percentage of 6.5-7 wt.%. The added water was weighted in a *Oertling* VA 204 series electric balance with a maximum capacity of 200 g and a minimum readability of 0.0001 g.
After a couple of minutes of mixing the consistency of the mixture started to change and homogenize resulting in a paste with the consistency resembling that of a non-Newtonian fluid (figure 43). The flowability of the cement can be tested using various methods, although in this study the flow table test was the one utilized to obtain the Flow Index (FI) of the created cements.

Figure 43. On the left the stand mixer used. On the right the final consistency of the wet mixture.

The flowability of the cement can be tested using various methods, although in this study the flow table test according to the ASTM C230 standard was the one utilized to obtain the Flow Index (FI) of the created cements. This test consists of filling a truncated inverted cone with the cement on a levelled table and after 30 seconds without disturbance (no vibration or compression) the cone is lifted in a motion perpendicular to the table (figure 44). After approximately 30 seconds the circumference of the flowing cement is taken, and the FI calculated using the initial and final diameter (equation 7). Common values to look to in the industry, for an initial diameter of 100 mm, are a final diameter of 150mm after 30 seconds for a cement without the need of vibration to be worked, and 200 mm after 30 seconds for a cement that can be pumped, for values higher than those the mixture runs the risk of suffering segregation [52].

$$FI = \frac{(D_{final} - D_{initial})}{D_{initial}} \times 100 \qquad (7)$$

Figure 44. Flow index table test. From left to right: Test cone positioned in a levelled table with the wider end pointing down, then test the cone is filled with the cement to be tested, the test cone is lifted vertically and after 30 seconds the diameter of the cement is marked and measured.

The cone used had an internal diameter on its wider end of 81 mm.

The paste is then poured into the nozzle mould and the excess in bars moulds that later will be used to test the mechanical properties of the refractory ceramic (figure 45).

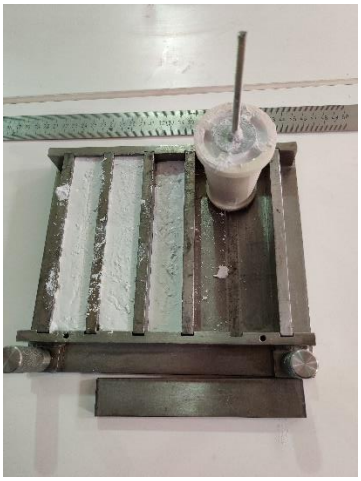

Figure 45. Filled nozzle and bars moulds.

The moulds were then vibrated (figure 46) as to remove air pockets that may have formed in their interior.

Figure 46. Filled moulds in a vibrating table to remover potential air pockets.

The filled moulds are left to dry overnight before demoulding. After which the pieces are put into a 60-degree Celsius kiln as shown in figure 47.

Figure 47. Alumina nozzle and bars in a 60 ºC kiln to curate.

The nozzles are then given a coating to obtain a smoother and less porous interior surface. This is made by creating a particle suspension (figure 48) in distilled water with 40% solids. The solid utilized were the same that were used in the alumina mixture with exception to the bigger sized particles as these would just sink and add nothing to the coating. The percentage of the 0.2-0.6 mm tabular alumina material was then distributed between the 0-0.2 mm and the -230-mesh tabular alumina. The final mixture of solids utilized in the coating mixture was then 30% reactive alumina, 36.5% AT 0-0.2 mm and 33.5% AT -230 mesh.

The 500 grams of distilled water are placed in a container on top of a digital magnetic heating stirrer (lbx instruments H03D series) and heated to 60ºC, while stirring the 200g (40 wt.%) of dry mixture is added along with a couple of drops of an alumina dispersant (dolapix ce 64).

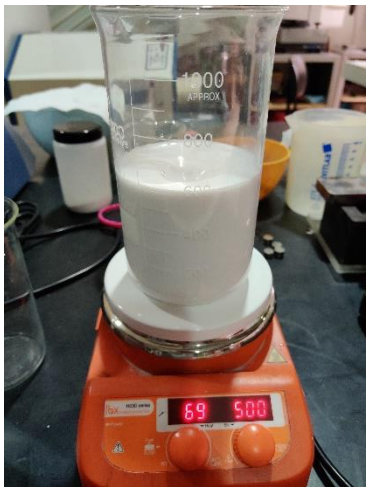

Figure 48. Particle suspension on a magnetic stirrer.

The nozzles are then submerged in the mixture and let to dry (figure 49). This submerging and drying process is repeated three to five times until the surface is deemed acceptable.

Figure 49. Submerging of the nozzles in the particle suspension.

Before sintering, and therefore hardening the material, the nozzle tops are sanded down to remove imperfections and thus allow a better connection to the rocket engine when testing. This process is made with a 400-grade sandpaper in a wet rotating plate (Struers DAP-V round polisher). This is displayed in figure 50.

Figure 50. Sanding table and nozzles before and after sanding.

Finally, the nozzles are ready for sintering. As the nozzles are almost fully composed of alumina (fusion at ~2000 ºC), they are placed in a furnace at 1500 ºC (around 80% of the maximum material temperature) overnight. The final product is shown in figure 51.

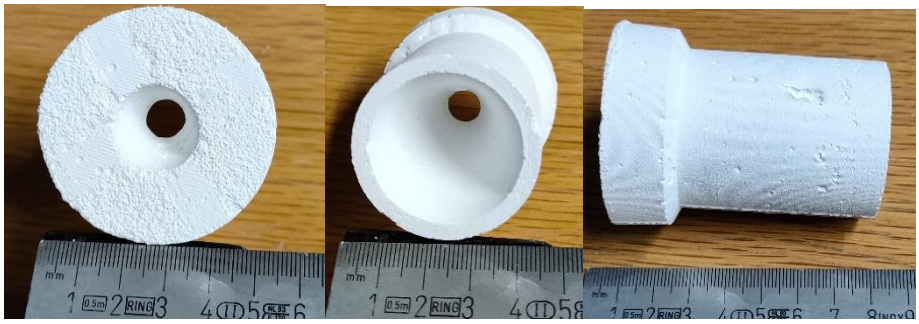

Figure 51. Final ALU nozzle.

4.4.1.2 ASH and PAN nozzles

The fabrication of the waste materials nozzles starts in a similar way to the alumina ones. The dry materials are weighted into a bowl following the percentages presented on table 17. Following the weighting, the 1 kg dry mixture is placed in a stand mixer and stirred. While being stirred the distilled water is weighted and slowly poured into the dry mixture. In this case the water content is 8.5 – 9 wt.%.

Due to the different materials utilized the final hydrated mixture didn't have self-flowing properties, having instead a spherical agglomerated appearance as seen in figure 52.

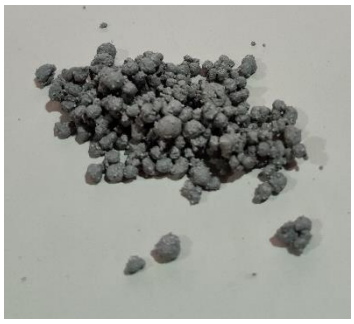

Figure 52. Consistency of the PAN and ASH hydrated mixture.

These agglomerates can however be broken up and can be made to form a homogeneous cement by working with small quantities at a time and applying some pressure during the moulding procedure.
The filled mould is then let to dry at room temperature overnight before being demoulded (figure 53).

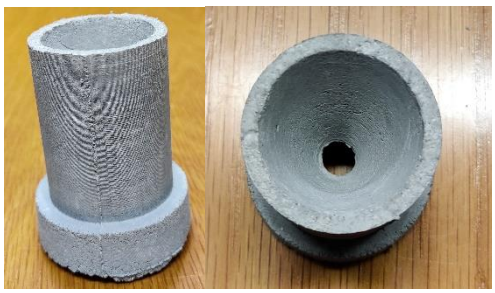

Figure 53. Demoulded PAN and ASH mixture nozzle.

As these nozzles were found to have a smooth enough interior surface, there was no need to apply a coating as it was made for the alumina ones. Furthermore, after testing it, the waste material nozzles were found to lose material from the extremities when submerged.
Thus, the coating step was skipped, and the nozzles were sanded before being sintered.
However, before sintering the nozzles, the bars were tested at different temperatures, as the fusion temperature of the ASH and PAN mixture was not known beforehand. The first try was made at 1200 ºC, and the following were increased in 100 ºC increments until 1500 ºC were reached. The difference between the sintering temperatures can be seen in figure 54.

Figure 54. From left to right: 1200 ºC, 1300 ºC, 1400 ºC and 1500 ºC PA material sintering temperature test bars.

Measurements were taken of the length of the bars after the process and signs of creep were looked for. The initial length of the bars was 152mm and the lengths after the sintering process at each temperature were as follows in table 18:

Sintering temperature (ºC)	**Length (mm)**
1200	151.4
1300	149.4
1400	149.3
1500	148.5

Table 18. Post sintering temperature test bar length.

The objective is to find the higher temperature possible without compromising the geometry of the sintered materials.

The temperature of 1400 ºC was found to be the highest the material could withstand, since, as the table and subsequent image show, at 1500 ºC the bar not only shrank to 148.5 mm, but it also bent under its own weight during the process as shown by the visible gap between the centre of the bar and the surface of the table (figure 55).

Figure 55. Right: 1400 ºC sintered bar. Left: 1500 ºC sintered bar with noticeable bend.

The nozzles and bars were then sintered at 1400 ºC as that was found to be the higher temperature at which the material can be sintered without suffering major volumetric alterations. The final PA nozzle is shown in figure 56.

Figure 56. Final PA nozzle.

4.4.2 Nozzle fabrication challenges

Alumina mixture nozzle

During the process of manufacturing the nozzles difficulties appeared that needed to be overcome. Although the exterior part of the mould could be easily removed from the dried cement, the interior could not.

During the first attempt at fabricating the nozzle, there was an attempt to use the minimum cement percentage possible, which in the final mixture was 0,1% instead of the later used 1% (1 g instead of 10 g). This coupled with the fact that the mould was not greased to facilitate the demoulding process, meant that this first try ended in a broken nozzle piece.

The next attempt was made with all the correct ratios of materials in the mixture. Furthermore, the mould was greased with machine oil to try and get the interior pieces of the mould to come apart from the dried cement. Once again, the exterior parts of the mould were easily demoulded while checking that the interior pieces were still resisting coming apart, the nozzle was put into a 60 ºC kiln with the interior mould pieces still inside to try and loosen the remaining mould pieces from the nozzle. This resulted although after checking the interior of the mould, it was verified that there was the formation of holes and cracks as seen in figure 57.

Figure 57. Cracks and holes on the early iteration ALU nozzles.

Attempt number three followed a similar process to that of number two with the differentiating factor that the mould was filled in three stages and vibrated in between each one, with the objective of reducing the air pockets formed. This resulted in that there were no major holes (internal porosity) formed in the interior of the nozzle. However, it remained impossible to demould the interior pieces without placing the piece in the kiln. From the second attempt there was also the possibility that by placing the nozzle with the ABS plastic inside the kiln, due to different thermal expansion ratios, it might contribute to the formation of cracks, mainly in the thinner section of the nozzle. As such the alumina nozzle number 3 was put into the kiln at a lower temperature (50 ºC) in 15-minute intervals, until it was feasible to demould the interior pieces. This still resulted in the appearance of cracks in the exit section of the nozzle which led to the nozzle ultimately breaking when trying to remove the interior mould.

For the fourth nozzle it was tested the insertion of the interior mould pieces in latex film before the pouring of the cement. The entire mould was also oiled. This approached showed promise as all pieces were easily demoulded, however due to the conical shape of the interior pieces as well as lack of options to keep the latex tight and in place, it ended up sinking into the cement and thus creating imperfections in the interior part of the nozzle (figure 58).

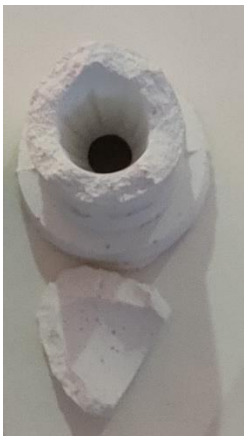

Figure 58. Latex film imprint on the nozzle interior surface.

For the fifth attempt the previous process was again tried as it showed promises, with the alteration that the latex film was fixed with adhesive tape to the threaded rod that transverses the

mould in the middle. This did make the imperfections less severe, although it also made removing the threaded rod very difficult which ended up breaking the nozzle piece.
In the 6th try, plastic film (cling film) was used instead of the latex as the crinkles were found to be smaller, which would allow for the interior texture of the nozzle to be improved by sanding after the firing. This did enable the demoulding of the interior pieces of the mould with minor imperfections. However, some minor cracks were found in the interior of the nozzle that may relate to a deficiency in the filling of the mould. Nevertheless, this last method was found to be a satisfactory solution to the demoulding process. The evolution of the ALU nozzle fabrication is seen in figure 59.

Figure 59. Various attempts (in chronological order from left to right) at the alumina nozzle fabrication.

ASH and PAN mixture nozzle

For the first try at making a nozzle with the ASH and PAN materials mixture, the particle packing was shown to not be satisfactory enough as the mixture ended up not having a self-flowing capability which made the filling of the mould almost impossible. It was also used higher quantities of water (15%) to try to confer some fluidity to the ceramic paste, this was found to hinder the quality of the mixture.
The second attempt was made with altered mixture quantities and lower water quantities (8%). This resulted in a mixture that was looser and had to be packed with some pressure applied. After mixing a layer of alumina paste formed at the bottom of the mixing bowl that might have contributed to the looser consistency of the mixture (figure 60).

Figure 60. Loose consistency ceramic paste dryed nozzle.

In the 3rd try, the cement quantity was double from 1% to 2% and the reactive alumina lower from 25% to 24%, furthermore, the reactive alumina (finer particles) was added last to the mixture to try and avoid the formation of the separated layer that appeared in the last effort. This resulted in a more homogeneous mixture, but still rather dry instead of a paste, as such the cement, nonetheless, needed to be packed by applying pressure to be able to be moulded. This resulted in a more cohesive nozzle piece but still quite brittle, mainly in the exit zone where the walls are finer.

From this point, and with the packing of the exit zone of the nozzle with a finer tool, and the filling of smaller quantities at a time, the process filling process was considered quite optimized. Still, when demoulding the divergent piece of the mould, the nozzle was found to consistently break. This was corrected by the removal of this piece immediately after the filling of the nozzle was done, and thus, before the refractory paste dried. As this mixture wasn't self-flowing, the shape was able to be maintained throughout the drying process. The different iterations of the PA nozzle fabrication process are displayed in figure 61.

Figure 61. Various attempts (in chronological order from left to right) at the ASH/PAN nozzle fabrication.

4.4.3 Sintered and green material properties

Having finished manufacturing of the nozzles and bars, tests were performed in order to better understand the properties of the resultant ceramic from the presented mixtures, as well as to study the way in which the material was altered by sintering (figure 62).

In this section the testing procedure is presented while the results obtained will be presented in the results chapter.

Figure 62. Left: Pre-sintered ALU bar fracture surface. Right: Sintered ALU bar interior.

4.4.3.1 Linear retraction

As previously discussed, the volumetric stability of refractory materials when exposed to high temperatures is a must. Not only can the material be damaged by the thermal expansion and contraction it suffers but it can also be damaging to its application.
Alumina refractories are known to contract during service [52], so it is of interest that the sintered bars are studied regarding their alteration is size after sintering, especially as the larger particle size distribution allows for a more stable structure to be expected.
The linear retraction test is utilized to evaluate the volumetric stability of a material. The testing of the material's linear retraction was done in accordance with the ASTM C-113 standard, and the values obtained from the following equation 8:

$$LR\ (\%) = \left|\frac{(Length_{final} - Length_{initial}}{Length_{initial}}\right| \times 100 \qquad (8)$$

The initial length is considered as the length of the bars after demoulding and the final is measured after the sintering process of bars. The measurements were taken from 5 different bars for each material with a *Powerfix Profi* digital calliper with a maximum resolution of 0.01 mm.

4.4.3.2 Apparent porosity

The porosity of a material is dependent of its manufacturing process, and mainly of the particle sizes selected. Furthermore, the porosity of a material determines its applications, higher porosity materials are better suited to applications as insulators, while eletrofused refractories can have porosity values almost null, giving them better mechanical properties.
Likewise, apparent porosity, water absorption, and bulk density are primary properties of refractory materials and widely used as a comparison metric for product and fabrication quality [53].
Not only the apparent porosity but the bulk density, water absorption, and apparent density were tested based on the basis of the ASTM C-20 standard, on five samples from each material.
Three weight measurements were taken for each bar, one of the dry samples, the second of a sample after being saturated in water for 72 hours and the final one with the sample suspended in water after being saturated.
The apparent porosity (AP) of the materials was calculated using the difference between the saturated and dry weights, and suspended weights, of the bars, as seen in the following equation 9:

$$AP\ (\%) = \frac{(W_{saturated} - W_{dry})}{(W_{saturated} - W_{suspended})} \qquad (9)$$

This equation is equivalent to multiply the water absorption by the bulk density of the material.

4.4.3.3 Apparent specific gravity

The apparent specific gravity (ASG) of the bars was calculated using the weight values previously taken and the equation 10.

$$ASG\ (\frac{g}{cm^3}) = \frac{W_{dry}}{W_{dry} - W_{suspended}} \qquad (10)$$

4.4.3.4 Bulk density

The materials bulk density (BD) in grams per cubic centimetre, can be obtained by dividing the dry weight by the exterior volume, including pores or by the following equivalent equation 11:

$$BD\ (\frac{g}{cm^3}) = \frac{W_{dry}}{W_{saturated} - W_{suspended}} \qquad (11)$$

4.4.3.5 Water absorption

The water absorption (WA) capabilities of a material, conveys the weight of water absorbed in relation to the dry weight of the bar as shown in equation 12.

$$WA\ (\%) = \frac{W_{saturated} - W_{dry}}{W_{dry}} \times 100 \qquad (12)$$

4.4.3.6 Dynamic elastic modulus

The dynamic elastic modulus, as by the BS 1881-203:1986 standard [54], can be calculated by the equation 13, with the values of density, Poisson coefficient and ultrasonic wave propagation speeds of the material.

$$E_{dyn}(\frac{MN}{m^2}) = \rho \times V^2 \times \frac{(1+v)\times(1-2v)}{(1-v)} \qquad (13)$$

Where:

ρ (bulk density) [kg/m³] is the density of the material.

V [km/s] is the propagation speed of an ultrasonic wave through the material.

υ is the Poisson coefficient.

The density used was the already calculated bulk density, while the V is taken with a "*TICO* Proceq" ultrasonic instrument. The Poisson coefficient is considered to be 0.22 as this is the tabulated value for ceramic materials composed of 99% alumina [55].

4.4.3.7 Modulus of rupture

When looking at the different applications of refractory materials a common theme is the necessity for considerable mechanical properties to sustain the stresses inherent to the environments and missions these materials are used in.

By studying the modulus of rupture of both the "green" and sintered materials it is possible to not only analyse the effectiveness of the sintering process and the properties that it imparts on the ceramics, but also the ability of the final material to respond to mechanical stresses that it may find upon its application.

Five samples of both the "green" and sintered bars were then subjected to a three-point flexural test (figure 63)as described on the ASTM C-113-97 standard [56]. For this test a *Shimazu AGS-X* was used, with a maximum load of 10kN and with adjustable supports that were set to a 100mm distance.

The bars were placed as seen in the images and the maximum force until breaking was taken for each of the samples. With this and the dimensions of the bars taken the equation 14 can be used to calculate the modulus of rupture (MoR) of each bar.

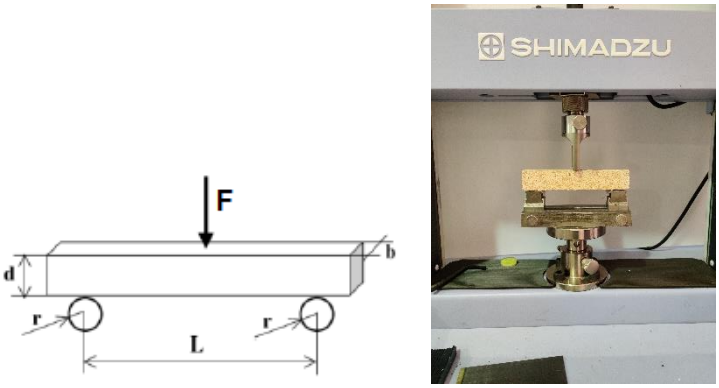

Figure 63. MoR three-point flexural test.

$$MoR\ (MPa) = \frac{3FL}{2bd^2} \qquad (14)$$

F is the maximum applied force during the test.

L is the distance between the bar supports.

b represents the width of the bar and d the thickness.

Chapter 5: Result analysis

5.1 Bar tests results

As mentioned in the previous chapter, bars were made from the same refractory materials used to make the nozzles and then tested.
In this section the results obtained by the characterization tests of the materials are numerically and graphically presented and discussed.
The standard deviation of all the independent samples is considered to be the measurement error and is going to be presented as such in this chapter.

5.1.1 Fluidity index

For the alumina refractory paste, due to its self-flowing properties, it was possible to evaluate its fluidity index.
Using equation 7 and the different measurements taken from the refractory pastes of the various samples tested, the following results were achieved (table 19).

Sample	Initial Diameter (mm)	Final Diameter (mm)	IF (%)
ALU 1	81	119	46.91
ALU 2	81	119	46.91
ALU 3	81	119	46.91
ALU 4	81	102	25.93
ALU 5	81	114	40.74
ALU 6	81	102	25.93
ALU 7	81	115	41.98
ALU 8	81	114	40.74
ALU 10	81	119	46.91
ALU 11	81	119	46.91
Average	**81 ± 0**	**114.20 ± 6.43**	**40.99 ± 7.94**

Table 19. Fluidity index results.

The initial diameter was constant for every test as this was the diameter of the truncated cone used in the test.
In terms of results, it is possible to see that one of the refractory paste mixtures is an outlier having smaller values of final diameter and fluidity index. This can be explained by the fact that in the

fabrication of this paste a slightly lower water content was used (6.2%) as this mixture in particular, acquired self-flowing properties and a homogenous appearance with a smaller amount of hydration. This mixture was also one of the first attempts at making the paste.
The remaining samples all scored a FI between 40-50% resulting in an average of approximately 41%, these samples also all had water contents of 6.5-6.6%.

In the case of the PA mixture, the refractory paste never reached a point of self-flowability or even of homogeneity, this meant that the FI wasn't able to be determined. This also implied that the filling of the mould had to be made and compacted by manually pressing the material into the mould as already explained in the nozzle fabrication section.

5.1.2 Linear retraction

After sintering the bars, the final length was measured and compared to the length before the sintering process. Using these measurements, the linear retraction was calculated (table 20).

Samples	Initial Length (mm)	Final Length (mm)	LR (%)
ALU 1	152	149.79	1.45
ALU 2	152	149.82	1.43
ALU 3	152	150.06	1.28
ALU 4	152	150.17	1.20
ALU5	152	149.7	1.51
ALU average	**152 ± 0**	**149.91 ±0.18**	**1.38 ± 0.12**
PA 1	152	149.06	1.93
PA 2	152	149.5	1.64
PA 3	152	148.94	2.01
PA 4	152	148.9	2.04
PA 5	152	149.23	1.82
PA average	**152 ± 0**	**149.13 ± .022**	**1.89 ± 0.14**

Table 20. Linear retraction of the sintered refractory bars.

Even though the sintering temperature was 100 ºC lower, the contraction of the PA bars was slightly more significant than that suffered by the alumina ones.
In general, it is possible to conclude that both materials are volumetrically stable, as both suffered less than 2% shrinkage. This success in size stability can be attributed to the research made regarding the particle size distribution used in the fabrication of both materials.

5.1.3 Apparent porosity

The apparent porosity was measured with 24, 48 and 72 hours of soaking. The values shown in table 20 are presented as the average of the measurements taken across those three-time windows. The standard deviation between the three different values is considered as the error.
The results for the alumina refractory material samples are shown in table 21.
The tests were only made on the sintered bars as the material before the sintering process when in the presence of water would become rehydrated.

Sample	Dry weight (g)	Saturated weight (g)	Submerged weight (g)	Apparent Porosity (%)
ALU 1	202.25	209.24 ± 0.13	146.71 ± 0.02	11.18 ± 0.18
ALU 2	196.07	202.88 ± 0.24	142.42 ± 0.06	11.27 ± 0.36
ALU 3	224.45	232.05 ± 0.04	163.19 ± 0.04	11.03 ± 0.05
ALU 4	233.47	241.68 ± 0.06	169.52 ± 0.07	11.38 ± 0.08
ALU 5	274.62	283.48 ± 0.09	199.24 ± 0.04	10.51 ± 0.10
Average	**-**	**-**	**-**	**11.07 ± 0.36**

Table 21. Weights and apparent porosity of the sintered ALU samples after 72 hours.

Due to the study of the particle size distribution of the mixture through the mixture packing model software, as well as the utilization of commercial grade alumina, the apparent porosity of the material besides being relatively low, is consistent across the different batches of the mixture produced.
The apparent porosity was projected to be relatively low, mainly, in order to improve the strength of the refractory material, and consequently of the nozzles, and with the added benefit of increasing the thermal conductivity of the material which allows for some heat transference between the outer surface of the nozzle and the surrounding air, thus somewhat dampening the thermal load suffered by the interior surface.
Due to the measuring of the mass of the samples across the three days it is possible to note that the weight variation, indicating water absorption, from 24 hours to 72 hours was slight. This indicates that the majority of the pores were filled with water in the first day of submerging.

Table 22 shows the results of the same apparent porosity test in the PA samples.

Sample	Dry weight (g)	Saturated weight (g)	Submerged weight (g)	Apparent Porosity (%)
PA 1	241.70	249.02 ± 0.47	167.84 ± 0.18	9.02 ± 0.54
PA 2	222.05	230.92 ± 0.28	154.48 ± 0.20	11.60 ± 0.34
PA 3	253.83	261.11 ± 0.36	176.77 ± 0.16	8.63 ± 0.39
PA 4	228.23	235.84 ± 0.20	158.47 ± 0.17	9.83 ± 0.25
PA 5	242.10	252.98 ± 0.38	168.65 ± 0.27	12.90 ± 0.43
Average	**-**	**-**	**-**	**10.39 ± 1.67**

Table 22. Weights and apparent porosity of the sintered PA samples after 72 hours.

There can clearly be seen in the results the impact that the increased randomness of the particles of the waste and ash materials has in the consistency of the material porosity by the bigger errors. Furthermore, it must be taken into account that the filling of the moulds with the PA material had to be made by manually applying pressure on the material, which inherently leads to inconsistencies. In addition to these factors, additional discrepancies from one material fabrication iteration to another, as well as between bars of the same batch, as the mixture was found to dry rather quickly, meaning the first moulded bar was easier to compact that the last.
The manual packing of the refractory paste into the moulds also led to, in average, lower apparent porosities than those obtained in the ALU bars.
The variation in weight from 24 to 48 to 72 hours were also found to be larger.

5.1.4 Apparent specific gravity

The apparent specific gravity of the samples was taken using the same measured weights used to study the apparent porosity, across 24, 48 and 72 hours.
First are presented the alumina results in table 23 and for the PA samples in table 24.

Samples	Apparent Specific Gravity (g/cm^3)
ALU 1	3.64 ± 0.00
ALU 2	3.65 ± 0.00
ALU 3	3.66 ± 0.00
ALU 4	3.65 ± 0.00
ALU 5	3.65 ± 0.00
Average	**3.65 ± 0.01**

Table 23. Apparent specific gravity of the ALU samples after 72 hours.

The results obtained were very consistent, not only across the three days if measurements, but also, throughout the different samples.

Sample	Apparent Specific Gravity (g/cm^3)
PA 1	3.27 ± 0.01
PA 2	3.29 ± 0.01
PA 3	3.29 ± 0.01
PA 4	3.27 ± 0.01
PA 5	3.30 ± 0.01
Average	**3.28 ± 0.01**

Table 24. Apparent specific gravity of the PA samples after 72 hours.

The apparent specific gravity values obtained for the PA samples although slightly less than those of the ALU ones, are also very consistency.
The ASG of the PA bars is however lower than that of the ALU ones, which might be explained by the lower densities of the alternative waste materials, as the apparent specific gravity of a determined volume of refractory material compares the weight of the impermeable part of that volume to that of water of the same volume.

5.1.5 Bulk density

Also using the weights of the soaked bars taken across a three-day span, the bulk density results taken are presented in the following tables 25 and 26.

Samples	Bulk Density (g/cm^3)
ALU 1	3.23 ± 0.01
ALU 2	3.24 ± 0.01
ALU 3	3.26 ± 0.00
ALU 4	3.24 ± 0.02
ALU 5	3.26 ± 0.00
Average	**3.25 ± 0.01**

Table 25. ALU material bulk density after 72 hours.

The values of the bulk density, although not as much as the ASG, are still very consistent across the three days as well as from sample to sample.
The bulk density of the ALU bars is, as expected, lower than that of its constituent materials.

Samples	Bulk Density (g/cm^3)
PA 1	2.98 ± 0.01
PA 2	2.90 ± 0.01
PA 3	3.01 ± 0.01
PA 4	2.95 ± 0.01
PA 5	2.87 ± 0.01
Average	**2.94 ± 0.05**

Table 26. PA material bulk density after 72 hours.

The PA samples are also extremely even in values of BD, and as anticipated lower than those of the ALU ones, in accordance with the less dense alternative waste materials used.
The bulk density represents the weight to volume ratio of the samples and is therefore dependant on the refractory materials used but also on the porosity and imperfections of the components.

5.1.6 Water absorption

Water absorption (tables 27 and 28) as the name suggests, keeps track of the percentage of water the sample absorbed by comparing its dry weight to its weight after being soaked. The measurements used were taken from the same three-day soaking process.

Sample	Water Absorption (%)
ALU 1	3.46 ± 0.06
ALU 2	3.47 ± 0.12
ALU 3	3.38 ± 0.02
ALU 4	3.52 ± 0.02
ALU 5	3.23 ± 0.03
Average	**3.41 ± 0.12**

Table 27. ALU samples water absorption percentage after 72 hours.

Sample	Water absorption (%)
PA 1	3.03 ± 0.19
PA 2	3.99 ± 0.13
PA 3	2.87 ± 0.14
PA 4	3.33 ± 0.09
PA 5	4.49 ± 0.16
Average	**3.54 ± 0.63**

Table 28. Water absorption percentage of the PA samples after 72 hours.

When comparing the two sample pools it is important to note the small difference in average between the ALU and PA materials. However, the PA samples present a greater variation among themselves, these inconsistencies between bars have been given possible explanations before.
Nevertheless, the relatively low water absorption values of both materials are intrinsically connected to those of the apparent porosity, as supported by comparing the individual samples by AP and WA (lower apparent porosity samples have lower water absorption percentages), particularly when considered that it is also related to the open porosity of the refractory materials.

5.1.7 Dynamic elastic modulus

The elastic modulus of a nearly pure alumina ceramic is calculated with a Poisson coefficient of 0.22 and is expected to be around 380 GPa, the value of the dynamic elastic modulus is dependent of the tested material porosity, thus values closer to 406 GPa also be common for high alumina ceramics [57].
To test the dynamic elastic modulus, an ultrasonic machine was used to assess the sound wave propagation velocity through the bars.
Three measurements were taken from each bar to minimize reading errors. The dynamic elastic modulus was calculated in MN/m^2 but is presented in GPa in tables 29 and 30.

Sample	Time (µs)	Velocity (m/s)	Dynamic Elastic Modulus (GPa)
ALU 1	20.70 ± 0.00	7250 ± 0.00	387.97 ± 0.73
ALU 2	20.70 ± 0.00	7250 ± 0.00	388.96 ± 1.18
ALU 3	20.67 ± 0.05	7260.00 ± 14.14	392.08 ± 0.47
ALU 4	20.60 ± 0.16	7280 ± 57.15	391.29 ± 0.31
ALU 5	20.07 ± 0.24	7476.67 ± 89.57	415.88 ± 0.30
Average	**20.55 ± 0.28**	**7303.33 ± 99.64**	**395.24 ± 10.45**

Table 29. Dynamic elastic modulus in GPa of the ALU.

The average value of the dynamic elastic modulus that resulted from the test of the ALU bars is close to the values that can be expected from high alumina content ceramics, and even more so the values of the ALU 1 and 2 samples were the propagation velocity was constant across the three measurements taken.

Sample	Time (µs)	Velocity (m/s)	Dynamic Elastic Modulus (GPa)
PA 1	22.80 ± 0.29	6583.33 ± 83.80	294.45 ± 1.25
PA 2	23.90 ± 0.22	6276.67 ± 55.58	261.17 ± 0.89
PA 3	21.70 ± 0.00	6910.00 ±0.00	327.94 ± 1.34
PA 4	22.57 ± 0.21	6650.00 ± 61.64	297.72 ± 0.71
PA 5	24.50 ± 0.16	6120.00 ± 40.82	245.39 ± 0.58
Average	**23.09 ± 1.01**	**6508 ± 285.33**	**285.34 ± 29.11**

Table 30. Dynamic elastic modulus in GPa of the PA mixture.

As it was to be expected, the dynamic elastic modulus of the PA samples is lower than that of the ALU ones. Furthermore, there were more and bigger variations both in velocities and the dynamic elastic modulus, this can be partly explained by the inconsistency related to the packing methodology applied due to the lack of self-flowing capabilities of the refractory material.
Additionally, the very probable formation of vitreous phase spots due to the alumina-silicate composition of the waste materials, which have significantly lower elastic modulus values, contributes to the overall lower values of elastic dynamic elastic modulus of the PA bars [58].

5.1.8 Modulus of rupture

To obtain the modulus of rupture (tables 31, 32, 33 and 34) of the test bars, as shown in the last chapter, the samples were submited to a three-point flexural test from which the maximum forces applied before the samples breaking point were taken.
In order to establish a reference, and to study the alteration of properties suffered by the material after the sintering process, the “green” samples were also submitted to the same test.
Some difference in values of maximum force (F) were expected as the bars have varying dimensions of thickness (d) and width (b).

Sample	L (mm)	b (mm)	d (mm)	F (N)	MoR (MPa)
ALU 1	100	15.72	26.54	4564.38	61.83
ALU 2	100	14.68	26.66	5440.6	78.22
ALU 3	100	16.81	26.64	5482.83	68.94
ALU 4	100	17.84	26.5	6284.54	75.25
ALU 5	100	21.49	26.46	8138.8	81.14
Average	**100 ± 0.00**	**17.31 ± 2.34**	**26.56 ± 0.08**	**5982.23 ± 1207.91**	**73.07 ± 6.92**

Table 31. Sintered ALU material mixture MoR.

The results of the ALU samples after sintering show high values of modulus of rupture, with an average value of 73 MPa.

Sample	L (mm)	b (mm)	d (mm)	F (N)	MoR (MPa)
ALU 6	100	19.96	26.43	554.92	5.97
ALU 7	100	20.02	26.91	307.75	3.18
ALU 8	100	18.71	25.52	435.85	5.37
ALU 10	100	15.87	27.02	311.52	4.03
ALU 11	100	16.7	27.13	254.19	3.10
Average	**100**	**18.25 ± 1.69**	**26.6 ± 0.59**	**372.84 ± 108.81**	**4.33 ± 1.16**

Table 32. Pre-sintering ALU material mixture MoR.

Comparing the results of the sintered samples to those of the pre-sintered material, the difference in the resistance of the material is overwhelming. The average of the “green” bars was of a modest 4.33 MPa for the MoR, this means that the sintering process led to an improvement in the material’s MoR of almost 17-fold.

The same test was run on the PA samples, both “green” and sintered.

Sample	L (mm)	b (mm)	d (mm)	F (N)	MoR (MPa)
PA 1	100	19.38	26.51	4753.39	52.35
PA 2	100	18.66	26.88	3319.52	36.93
PA 3	100	20.60	26.64	4626.46	47.47
PA 4	100	19.18	26.64	3411.77	37.60
PA 5	100	20.18	26.47	3135.02	33.26
Average	**100 ± 0.00**	**19.6 ± 0.7**	**26.63 ± 0.14**	**3849.23 ± 693.35**	**41.52 ± 7.17**

Table 33. MoR of the sintered PA bars.

As expected, the alternative materials samples didn't generally reach the same values of force or MoR. However, there were still reached values of significant resistance. The average modulus of rupture was of a respectable 41.52 MPa.

Sample	L (mm)	b (mm)	d (mm)	F (N)	MoR (MPa)
PA 6	100	19.65	27.09	87.82	0.91
PA 7	100	19.55	26.92	90.47	0.96
PA 8	100	19.04	26.95	78.78	0.85
Average	**100 ± 0.00**	**19.41 ± 0.27**	**26.99 ± 0.07**	**85.69 ± 5.01**	**0.91 ± 0.04**

Table 34. Pre-sintered PA bars MoR.

The "green" PA samples on the other hand presented very low values of both force and MoR. The brittle material reached an average MoR lower than 1 MPa. Even when compared with the pre-sintering bars of ALU the values were still very low, which gives extra credit to the values of MoR and F attained for the sintered PA bars.

The increment in the average MoR of the samples increased by almost 46 times.

This means that the MoR increase by the sintering of the material in the PA case was 2.7 times higher than in the ALU samples, even though the sintering temperature had to be 100ºC lower.

Chapter 6: Conclusions and future studies

6.1 Conclusions

At the beginning of this document, there were several objectives proposed, the first being to better comprehend refractory materials and their general applications, and in specific in the aeronautical and aerospace industries and with a greater focus on the possibility if using these types of materials in a rocket nozzle. With the development of the state of the art and furthermore with the study cases, it is possible to better comprehend not only the role that refractory ceramics play, but also to understand the basics of rocket propulsion. Moreover, it was skimmed over the various types of materials and their inherent characteristics, and their applications in the relevant industries to this study. Ways of studying and distinguishing their characteristics and properties were also given.

Nevertheless, the emphasis was obviously placed on refractory ceramic materials and their constituents, properties, utilizations, and manufacturing and fabrication processes, such as the particle packing models that allowed for a homogeneous and volumetrically stable material even when subjected to large temperature variations.

In the practical chapters of this dissertation two 3D printed moulds were produced using the CAD software Fusion 360 to design of these, besides, some focus was put into the function of this piece as well as the ease of utilization. Steps were taken to guarantee the concentricity of the mould pieces in relation to each other, as the symmetry of the nozzle was a critical point, as shown in the study cases. Also, the demoulding was though of while designing the mould, the ability to reutilize the mould for various nozzles was a must, as such the removal of the nozzle had to be able to be made without damaging the 3D printed mould. More than the removal of the divided exterior pieces, it was known that the interior ones would prove challenging, these were projected to be separated as well, and moreover designed with a threaded interior to allow for a better gripping surface, thus allowing to be pulled from the interior of the dried nozzles.

Once the moulds were printed, the first material was chosen to be an almost pure alumina mixture, due to the state of the art this material was known to be a good starting point and comparison to any other chosen material. These also meant that the mixture could be made using commercial grade materials which facilitated the manufacturing process leaving the attention to be mainly placed in the mould filling and demoulding of the piece as well as the correction of any imperfection that might occur. Having successfully developed a methodology which allowed for fairly consistent results, the second mixture materials were chosen. At this point the challenge appeared to use alterative materials such as the Panasqueira mine surplus and the Pego thermoelectric fly-ash by product and therefore study a possible reutilization of these otherwise wasteful materials. These materials were evidently not as refined as the commercial alumina, which led to a different set of challenges in the manufacturing process. Nevertheless, the

fabrication of both the mixture and the respective nozzles can be considered a success as test worthy nozzles were obtained regularly by the end.
Thus, having studied the materials and achieved a reliable manufacturing process of the nozzles the next objective was to study the quality of the fabrication of the nozzles through the properties of the obtained refractory ceramics.
To achieve this several tests were performed on the materials test bars.
With the tests it was possible to understand that the manufacturing process resulted in fairly consistent material properties, especially with regard to the apparent porosity, 11% for the ALU samples and 10% for the PA ones, apparent specific gravity, 3.65 and 3.28 g/cm^3 for the ALU and PA bars respectively, and bulk density, 3.25 g/cm^3 of the ALU samples and 2.94 g/cm^3 of the PA samples. The dynamic elastic modulus of the ALU bars (average of 395 GPa) was also in accordance with the expected for high content alumina ceramics which again spoke to the success of the fabrication process. The inconsistency of the PA materials particle size as well as some possible spots of material in a vitreous phase explain the lower values of the dynamic elastic modulus (285 GPa average) obtained for the alternative material.
The same occurs with the MoR, where the ALU samples performed, as expected, significantly better achieving an average MoR of 73 MPa, versus the 42 MPa MoR of the PA bars. However, both materials, when considering the grade of raw materials used, performed according to what was hope for, achieving significant values of MoR and therefore being deemed rather successful properties wise.

6.2 Future studies

Having completed this study, opportunities appear for the completion and the development of new hypothesis such as:

- The testing of the nozzles mounted on a rocket engine and post-mortem study of the materials.
- Development of different nozzle geometries in order to study the influence, if any, the geometry may have on the material ability to deal with the extreme rocket propulsion environment.
- Refinement of the particle size distribution of the mines waste and fly-ash in order to be able to utilize bigger quantities of these materials without having imbalances in the granulometry of the mixture.
- Study of the micro-structure alterations that occur on the waste refractory material, mainly the probable formation of vitreous phase spots.
- Research the ability of developing a self-flowing refractory paste using the mine waste and fly-ash.

- Analyse the thermal shock and thermal cycle response of the alternative refractory material.
- Develop a numerical model (digital twin) to describe the reliability of the material in relation to the geometry and lifespan of the nozzle.

Bibliography

[1] D. A. Shearer and G. L. Vogt, “Rockets: A Teacher’s Guide with Activities in Science, Mathematics, and Technology,” Washington, DC., EG-1996-09-108-HQ, Sep. 1996.

[2] NASA, “Brief History of Rockets.” https://www.grc.nasa.gov/www/k-12/TRC/Rockets/history_of_rockets.html (accessed Jan. 22, 2023).

[3] M. N. bin Rosli, “Fabrication of ceramic nozzle made from clay-alumina mixture,” 2014.

[4] B. Nigar, S. Dönmez, D. Çöker, and S. Özerinç, “Understanding mechanical failure of graphite rocket nozzle throats under thermal stresses,” *Aerosp Sci Technol*, vol. 119, 2021, doi: 10.1016/j.ast.2021.107152.

[5] D. Y. Park, Y. J. Oh, Y. S. Kwon, S. T. Lim, and S. J. Park, “Development of non-eroding rocket nozzle throat for ultra-high temperature environment,” *Int J Refract Metals Hard Mater*, vol. 42, pp. 205–214, 2014, doi: 10.1016/j.ijrmhm.2013.09.007.

[6] A. H. O. Manna, M. A. A. Mohammed, M. E. E. Ahmed, and M. O. E. Ali, “Study of Refractory Materials Usage in Aerospace Engines Technology,” 2017.

[7] NASA, “Rocket Principles.” https://www.grc.nasa.gov/WWW/k-12/rocket/TRCRocket/rocket_principles.html (accessed Mar. 22, 2022).

[8] P. M. Sforza, *Theory of aerospace propulsion*, Second Edition. 2017.

[9] P. Merklinghaus, “Missile and Rocket Propulsion Review,” pp. 24–29, 2013.

[10] NASA, “Prop.” https://history.nasa.gov/conghand/propelnt.htm (accessed Jan. 22, 2023).

[11] F. Maggi, A. Bandera, L. Galfetti, L. T. De Luca, and T. L. Jackson, “Efficient solid rocket propulsion for access to space,” *Acta Astronaut*, vol. 66, no. 11–12, pp. 1563–1573, 2010, doi: 10.1016/j.actaastro.2009.10.012.

[12] G. C. Oates and C. Gordon, *Aerothermodynamics of Gas Turbine and Rocket Propulsion Third Edition*. 1801.

[13] A. N. Buturache, “Performances study of a hybrid rocket engine,” *INCAS Bulletin*, vol. 10, no. 2, pp. 173–184, 2018, doi: 10.13111/2066-8201.2018.10.2.16.

[14] Daniel Rodriguez Lopez, “Booster Staging,” *NASA*, Jan. 11, 2018.

[15] P. M. Sforza, *Theory of aerospace propulsion*, Second Edition. 2017.

[16] S. Khare and U. K. Saha, “Rocket nozzles: 75 years of research and development,” *Sadhana - Academy Proceedings in Engineering Sciences*, vol. 46, no. 2, 2021, doi: 10.1007/s12046-021-01584-6.

[17] J. Singh, L. E. Zerpa, B. Partington, J. Gamboa, and L. E. Zerpa, “Effect of nozzle geometry on critical-subcritical flow transitions,” 2019, doi: 10.1016/j.heliyon.2019.

[18] N. Gayathri, P. Senthilkumar, K. Dineshkumar, M. Purusothaman, and B. Sriharan, “CFD analysis on flow through nozzle of conical type and truncated conical plug type,” *Mater Today Proc*, Oct. 2022, doi: 10.1016/j.matpr.2022.09.407.

[19] D. Schneider and C. Génin, “Numerical investigation of flow transition behavior in cold flow dual bell rocket nozzles,” in *51st AIAA/SAE/ASEE Joint Propulsion Conference*, 2015. doi: 10.2514/6.2015-4219.

[20] H. Kbab, M. Sellam, T. Hamitouche, S. Bergheul, and L. Lagab, “Design and performance evaluation of a dual bell nozzle,” *Acta Astronaut*, vol. 130, pp. 52–59, Jan. 2017, doi: 10.1016/j.actaastro.2016.10.015.

[21] K. R. Sreenath and A. K. Mubarak, “Design and analysis of contour bell nozzle and comparison with dual bell nozzle,” 2016.

[22] A. A. Alsayed, “Physics of Open Fractures: Reconsidering Tissue Viability, Contamination Risk and Importance of Wound Debridement,” *Journal of Applied Mathematics and Physics*, vol. 09, no. 01, pp. 176–182, 2021, doi: 10.4236/jamp.2021.91012.

[23] Matmacth, “What is fatigue strength.” https://matmatch.com/learn/property/fatigue-strength (accessed Jan. 05, 2023).

[24] A. Silva, “Propriedades comuns a observar nos materiais,” *Aulas de Materiais de Construção Aeroespacial, Mestrado Integrado Engenharia Aeronáutica, UBI*. 2022.

[25] X. Tardif *et al.*, “Experimental study of crystallization of PolyEtherEtherKetone (PEEK) over a large temperature range using a nano-calorimeter,” *Polym Test*, vol. 36, pp. 10–19, 2014, doi: 10.1016/j.polymertesting.2014.03.013.

[26] G. Solomon and Y. AlemayehuAdde (Kibret), “Design and analysis of rocket nozzle,” *IOSR Journal of Engineering (IOSRJEN)*, vol. 10, no. 5, doi: 10.1016/j.matpr.2020.10.370.

[27] “Polyimide Boosts High-Temperature Performance,” *NASA Spinoff*. Polyimide Boosts High-Temperature Performance (accessed Jan. 18, 2023).

[28] R. Harikrishnan and B. R. Lokavarapu, “Design and analysis of rocket nozzle,” *Mater Today Proc*, vol. 38, pp. 3365–3371, 2020, doi: 10.1016/j.matpr.2020.10.370.

[29] P. Boch and J.-C. Nièpce, *Ceramic Materials: Processes, Properties and Applications*. 2007.

[30] W. D. Callister, “Material Science and Engineer,” *J Mater Sci*, vol. 26, no. 14, pp. 3940–3944, 1991.

[31] K.-S. Kim, S.-H. Lee, V. Q. Nguyen, Y. Yun, and S. Kwon, “Ablation characteristics of rocket nozzle using HfC-SiC refractory ceramic composite,” *Acta Astronaut*, vol. 173, no. April, pp. 31–44, 2020, doi: 10.1016/j.actaastro.2020.03.050.

[32] L. N. Peng, G. Q. He, J. Li, L. Wang, and F. Qin, “Effect of combustion gas mass flow rate on carbon/carbon composite nozzle ablation in a solid rocket motor,” *Carbon N Y*, vol. 50, no. 4, pp. 1554–1562, Apr. 2012, doi: 10.1016/j.carbon.2011.11.034.

[33] J. Njuguna and K. Pielichowski, “The Role of Advanced Polymer Materials in Aerospace.”

[34] N. E. Prasad and R. J. H. Wanhill, “Aerospace Materials and Material Technologies, Volume 1: Aerospace Materials.”

[35] W. O. Soboyejo, J. D. Obayemi, E. Annan, E. K. Ampaw, L. Daniels, and N. Rahbar, “Review of High Temperature Ceramics for Aerospace Applications,” *Adv Mat Res*, vol. 1132, pp. 385–407, Dec. 2015, doi: 10.4028/www.scientific.net/amr.1132.385.

[36] T. E. Steyer, “Shaping the future of ceramics for aerospace applications,” *Int J Appl Ceram Technol*, vol. 10, no. 3, pp. 389–394, May 2013, doi: 10.1111/ijac.12069.

[37] M. Mrazova, “Advanced composite materials of the future in aerospace industry,” *INCAS BULLETIN*, vol. 5, no. 3, pp. 139–150, Sep. 2013, doi: 10.13111/2066-8201.2013.5.3.14.

[38] S. Mungiguerra, G. D. Di Martino, R. Savino, L. Zoli, L. Silvestroni, and D. Sciti, “Characterization of novel ceramic composites for rocket nozzles in high-temperature harsh environments,” *Int J Heat Mass Transf*, vol. 163, p. 120492, 2020, doi: 10.1016/j.ijheatmasstransfer.2020.120492.

[39] P. Boch and J.-C. Nièpce, *Ceramic Materials: Processes, Properties and Applications*. 2007.

[40] A. Bhatia, “Overview of Refractory Materials Section-6: Refractory Applications in Industry.” [Online]. Available: www.PDHcenter.comPDHCourseM158www.PDHonline.org

[41] “‘Aplicación de la ingeniería de sistemas complejos para el diseño de refractarios monolíticos y piezas preformadas; Lecture 9: Refractory Materials’, Technical course promoted to CYTED Network and ANFRE by HOREF Project, Madrid, Spain, 30 horas, 29/09/2014 – 2/10/2014.Lecture 9: Refractory Materials,” HOREF Project., Madrid, 2014.

[42] “‘Aplicación de la ingeniería de sistemas complejos para el diseño de refractarios monolíticos y piezas preformadas: Introduction to Refractory and Insulating Materials’, Technical course promoted to CYTED Network and ANFRE by HOREF Project, Madrid, Spain, 30 horas, 29/09/2014 – 2/10/2014.”

[43] “‘Aplicación de la ingeniería de sistemas complejos para el diseño de refractarios monolíticos y piezas preformadas; Lecture 15: Application of Refractory Materials’, Technical course promoted to CYTED Network and ANFRE by HOREF Project, Madrid, Spain, 30 horas, 29/09/2014 – 2/10/2014.”

[44] R. D’Elia, G. Bernhart, T. Cutard, G. Peraudeau, and M. Balat-Pichelin, “Preliminary tests of silicon carbide based concretes for hybrid rocket nozzles in a solar furnace,” *Acta Astronaut*, vol. 99, no. 1, pp. 242–251, 2014, doi: 10.1016/j.actaastro.2014.02.027.

[45] R. D’Elia, G. Bernhart, J. Hijlkema, and T. Cutard, “Experimental analysis of SiC-based refractory concrete in hybrid rocket nozzles,” *Acta Astronaut*, vol. 126, pp. 168–177, 2016, doi: 10.1016/j.actaastro.2016.04.034.

[46] S. Mungiguerra, G. D. di Martino, R. Savino, L. Zoli, L. Silvestroni, and D. Sciti, “Characterization of novel ceramic composites for rocket nozzles in high-temperature harsh environments,” *Int J Heat Mass Transf*, vol. 163, p. 120492, 2020, doi: 10.1016/j.ijheatmasstransfer.2020.120492.

[47] “Global Product Data Tabular Alumina T60/T64*.” Accessed: Jan. 03, 2023. [Online]. Available: www.almatis.com

[48] “Global Product Data CT3000LS SG.” [Online]. Available: www.almatis.com

[49] J. Coutinho Lanhoso Araújo Mamede, D. A. Manuel Pereira da Silva, and D. A. Maceiras Martinez, “Compósitos cerâmicos para sistemas de proteção térmica de aeronaves:- Análise do material CaZrO3-MgO-Al2O3.”

[50] S. C. Carniglia and G. L. Barna, *Handbook of Industrial Refractories Technology: Principles, Types, Properties and Applications*. New Jersey: Noyes Publications, 1992.

[51] “EMMA mix analyser.” [Online]. Available: https://www.elkem.com/silicon-products/refractories/emma/

[52] D. G. Pinto, “Comportamento Termomecânico de um Betão Refractário de 100% Alumina para Aplicações Monolíticas,” Universidade da Beira Interior, Covilhã, 2011.

[53] “ASTM C-20: Standard Test Methods for Apparent Porosity, Water Absorption, Apparent Specific Gravity, and Bulk Density of Burned Refractory Brick and Shapes by Boiling Water 1.” Accessed: Dec. 08, 2022. [Online]. Available: www.astm.org

[54] British Standards Institution., *BS 1881-203: Specification for testing concrete. Part 203. Recommendations for measurement of velocity of ultrasonic pulses in concrete.* British Standards Institution, 1986.

[55] Sonelastic, “Modulus of elasticity and Poisson’s coefficient of typical ceramic materials.” https://www.sonelastic.com/en/fundamentals/tables-of-materials-properties/ceramics.html (accessed Dec. 09, 2022).

[56] “ASTM C113-97: Standard Test Methods for Cold Crushing Strength and Modulus of Rupture of Refractories 1.” Accessed: Dec. 08, 2022. [Online]. Available: www.astm.org

[57] P. M. C. Carneiro, P. v. Gamboa, C. Baudín, and A. P. Silva, “Modelling of elastic modulus of a biphasic ceramic microstructure using 3D representative volume elements,” *J Eur Ceram Soc*, vol. 40, no. 3, pp. 901–910, Mar. 2020, doi: 10.1016/j.jeurceramsoc.2019.10.046.

[58] A. P. Silva, F. Booth, L. Garrido, E. Aglietti, P. Pena, and C. Baudín, “Young’s modulus and hardness of multiphase CaZrO3-MgO ceramics by micro and nanoindentation,” *J Eur Ceram Soc*, vol. 38, no. 4, pp. 2194–2201, Apr. 2018, doi: 10.1016/j.jeurceramsoc.2017.11.007.